
Article:
Yan, N orcid.org/0000-0003-1790-5861, Colombera, L orcid.org/0000-0001-9116-1800 and Mountney, NP orcid.org/0000-0002-8356-9889 (2020) Controls on fluvial meander-belt thickness and sand distribution: insights from forward stratigraphic modelling. Sedimentology. ISSN 0037-0746

https://doi.org/10.1111/sed.12830

Controls on fluvial meander-belt thickness and sand distribution: insights from forward stratigraphic modelling

NA YAN*[1], LUCA COLOMBERA[1], NIGEL P. MOUNTNEY[1]

1 – Fluvial & Eolian Research Group, School of Earth and Environment, University of Leeds, Leeds, LS29JT, UK
* n.yan@leeds.ac.uk; corresponding author

ABSTRACT
Fluvial point-bar evolution commonly involves multiple stages of bar development driven by changes in the style of meander transformations. Complicated planform morphologies are widely recognised in remote-sensing imagery, but the relationships between meander-bend evolutionary behaviour and stratigraphic architecture, facies distribution, and sand volumes remain poorly understood. This study applies a geometric forward stratigraphic model (PB-SAND) to simulate the internal sedimentary architecture of twenty-four meander-belt segments that evolved via a broad range of meander-bend transformation styles. Modelling inputs are constrained by channel trajectories inferred from high-resolution LiDAR datasets, lithological information from a sedimentological database (FAKTS), and geological knowledge of trends in point-bar lithology (e.g., decrease in sand proportion with sinuosity, downstream of bend apices, and beyond the transition from point-bar to counter-point-bar deposits) and in channel bathymetry (depth variations across pools and riffles). Modelling results are used to explore how the relative distribution of sand and mud is controlled by the styles of point-bar transformation, quantified by the relative degree of meander translation versus expansion, and by the amount of bend rotation. The 24 models are classified into three groups based on cluster analysis of their mean migration angle, mean apex rotation, mean sinuosity, standard deviation of channel circular variance, and preservation ratio; these quantities are known to be controlled by meander transformation types. Quantitative comparisons across these groups and relationships between metrics of planform change and quantifications of point-bar deposits demonstrate how meander planform evolution controls point-bar thickness and sand volume. Locally, the thickness of sand in bar deposits is controlled by the interplay of facies trends and spatial variations in bar thickness that reflect bathymetric changes, both related to local hydrodynamics. The proposed workflow establishes linkages between planform morphologies and three-dimensional facies distributions; it can be employed to characterise the distribution of subsurface porous volumes where the planform history of meander bends can be reconstructed.

KEYWORDS
point bar; meander transformation; meander rotation; sedimentary architecture; quantitative stratigraphy; numerical model

INTRODUCTION
As fluvial meanders evolve, they commonly undertake lateral expansion, downstream translation and apex rotation whereby the dominant direction of channel migration can change repeatedly through various stages of bar development (Makaske and Weerts, 2005; Jackson, 1976; Ielpi and Ghinassi, 2014; Ghinassi *et al.*, 2016). Through the alternation of stages of meander-bend expansion, translation and rotation, point-bar deposits accumulated in the earlier stages of bar development can experience multiple episodes of partial erosion, and this can give rise to sedimentary architectures characterised by the juxtaposition of lateral-

accretion packages with different accretion directions, as evidenced by complex mosaics of scroll-bar sets observed in planforms of modern rivers (Durkin *et al.*, 2015; Strick *et al.*, 2018; Durkin *et al.*, 2019; Johnston & Holbrook, 2019; Willis & Sech, 2019a). In parallel with variations in the dip azimuth and inclination of bar-accretion surfaces, bathymetric variations that exist along sinuous channels, such as depth changes across riffles and pools, may also cause variability in the thickness of channel-belt deposits in three-dimensions (Willis & Tang, 2010; Ielpi & Rainbird, 2015; Willis & Sech, 2019a). Point bars with complicated planform scroll-bar morphologies, testifying to complex evolutionary histories, are widely recognised in remotely sensed images of modern rivers (e.g., Strick *et al.*, 2018; Russell *et al.*, 2019). However, the relationship between meander-transformation behaviour, including rotational shifts of channel migration, and the resulting stratigraphic architecture and lithofacies distribution within point-bar bodies remains relatively poorly understood, largely due to limited outcrop or subsurface evidence (Thomas *et al.*, 1987; Miall, 1996; Nicoll & Hickin, 2010; Hooke & Yorke, 2011; Clift *et al.*, 2018; Parquer *et al.*, 2020). A detailed understanding of internal geometries and facies distributions of complex point-bar elements is important for reconstruction of past sedimentary environments of river meander belts to gain improved understanding of Earth history. In applied respects, such understanding can also assist in estimation of reservoir compartmentalisation arising from juxtaposition of volumes with contrasting lithologies, and prediction of spatial heterogeneity in sand volumes.

Several facies trends are recognised in fluvial point-bar deposits, as observed in modern rivers and ancient outcropping successions. A fining-upward trend commonly characterises fluvial point-bar deposits, in relation to energy dissipation associated with secondary helical flow in meander bends (Nanson, 1980; Bridge *et al.*, 1995). A fining-outward trend, i.e., an overall decrease in grainsize away from the initial inner bank on which the incipient point bar started to accrete as the meander underwent expansion, is seen for river bends that experience a marked increase in sinuosity, due to declining flow energy associated with a progressive decrease in streamwise gradient around the bend (Hickin, 1974; Piet, 1992; Miall, 1996; Durkin *et al.*, 2015). A downstream-fining trend can also develop, which is dependent upon bend curvature and is related to streamwise variations in the flow-velocity field (Bluck, 1971; Jackson, 1976; Wood, 1989; Deschamps *et al.*, 2011; Fustic *et al.*, 2012; Ghinassi *et al.*, 2016). Under some circumstances, typically in meander bends undergoing translation, the preservation of deposits accreting on the channel concave bank is possible, and these sediments, which are commonly termed ‘counter-point bar’ deposits, tend to be dominated by mud- or silt-prone lithofacies; their presence can further encourage meander translation (Jackson, 1976; Hickin 1979; Burge & Smith, 1999; ; Smith *et al.*, 2009; Nicoll & Hickin, 2010; Labrecque *et al.*, 2011; Ghinassi & Ielpi, 2015; Ghinassi *et al.*, 2016). Variability also exists in the bathymetry of sinuous river channels, whereby deeper pools tend to develop in proximity of meander apices, whereas shallower riffles form near channel inflection points (Bhowmik & Demissie, 1982; Milne, 1982; Thompson, 1986; Lofthouse & Robert, 2008; Hooke & Yorke, 2011). Consequently, point bars that accrete in response to the migration of bathymetrically variable channels are characterised by spatial variations in thickness; overall, bar deposits accumulated near the meander apex will tend to be thicker than deposits that accreted at the meander inflection (Willis & Tang, 2010; Ghinassi *et al.*, 2014; Willis & Sech, 2019a, b).

These mechanisms interact with each other, making predictions of channel-belt facies distribution and thickness variations, and in turn of point-bar sand volumes, a challenging task. The aim of this study is to explore how the preservation of sand deposits is controlled by the styles of point-bar transformation, relative degree of downstream translation versus expansion, and the direction and degree of rotation that is associated with changes in

autogenic dynamics that govern channel evolution. To achieve this, the following specific objectives are sought: (i) to devise a workflow that predicts 3D channel-belt architecture and preserved deposits using a forward stratigraphic model informed by established geological knowledge, remote-sensing data of modern rivers, and a sedimentological database of example fluvial systems; (ii) to model 3D sedimentary architecture and lithofacies distributions of point bars with different planform morphology and accretion patterns, arising from their unique growth history and associated style of meander transformation; (iii) to quantify the relationships between point-bar planform evolution and facies heterogeneity, bar geometry, and sand volume; and (iv) to predict sand distribution and volume of point-bar deposits based on knowledge of planform morphology and accretion style.

METHODOLOGY

Overview

The modelling workflow adopted in this work combines geometric- and process-based approaches and uses both deterministic and stochastic modelling. This workflow is followed to reconstruct the complex spatio-temporal evolution of portions of meandering-river channel belts, to quantify variations in 3D geometry and lithofacies distribution of point bars under different conditions of channel migration (Fig. 1). The modelling algorithm, PB-SAND (Point-Bar Sedimentary Architecture Numerical Deduction; Yan *et al.*, 2017, 2019, 2020; Colombera *et al.*, 2018), requires input parameters that allow the meander-bend transformation style and trajectory associated with bar growth to be specified.

Twenty-four meander-belt models were built that reflect the planform evolution observed in real-world examples from modern rivers, as captured in a selection of high-resolution LiDAR images that cover a broad range of meander-transformation styles, embodying different combinations of meander-bend expansion, translation and rotation of varying degrees (Fig. 2). LiDAR images by the United States Geological Survey and Geological Survey of Finland are used to illustrate natural analogues to the modelled planforms. This remote-sensing dataset was used to digitise current and former channel trajectories that track the geomorphic history of the studied river reaches; the evolutionary trajectories of these rivers are suitable as input to PB-SAND, which is itself used to model and reconstruct the sedimentary architecture and lithofacies distributions of point bars that evolve according to the same styles of morphodynamic evolution. Other parameters selected for constraining the model are informed based on data from studies of modern rivers and on sedimentological data extracted from a database of fluvial successions (FAKTS, Fluvial Architecture Knowledge Transfer System; Colombera *et al.*, 2012a, b). The planform morphology of the evolving meanders and the facies architecture of the associated point-bar deposits, as modelled by PB-SAND, have been analysed statistically, by considering metrics that describe: (i) point-bar planform shape and morphological evolution (i.e., channel sinuosity, accretion direction, meander rotation, and degree of sediment preservation); and (ii) 3D geometry and heterogeneity of point-bar deposits, particularly with respect to the spatial variability in thickness and sand fraction of point-bar deposits.

Input 1: channel trajectories

Trajectories that depict the past course of a river channel at specific times through different stages of point-bar evolution are interpreted and digitised based on the scroll-bar patterns found in the LiDAR images. The river reaches whose topography is characterised by the LiDAR data are employed as natural analogues to idealised rivers: the workflow does not aim to generate outputs that match in scale and lithological organisation with these examples (see below for details on scaling). Vector centrelines of these trajectories are used as input to PB-SAND (Yan *et al.*, 2017). Fig. 2 shows three example sets of centrelines; in each set –

i.e., for each meander-belt case study – the centrelines are assigned a relative chronological order (e.g., *t1* to *t6*, in Fig. 2A). The number of input trajectories is determined by the complexity of transformation styles that needs to be captured, for example in terms of degree of apex rotation or extent of point-bar reactivation. Patterns of point-bar lateral accretion are generated by PB-SAND through linear interpolation of these input trajectories (Yan *et al.*, 2017).

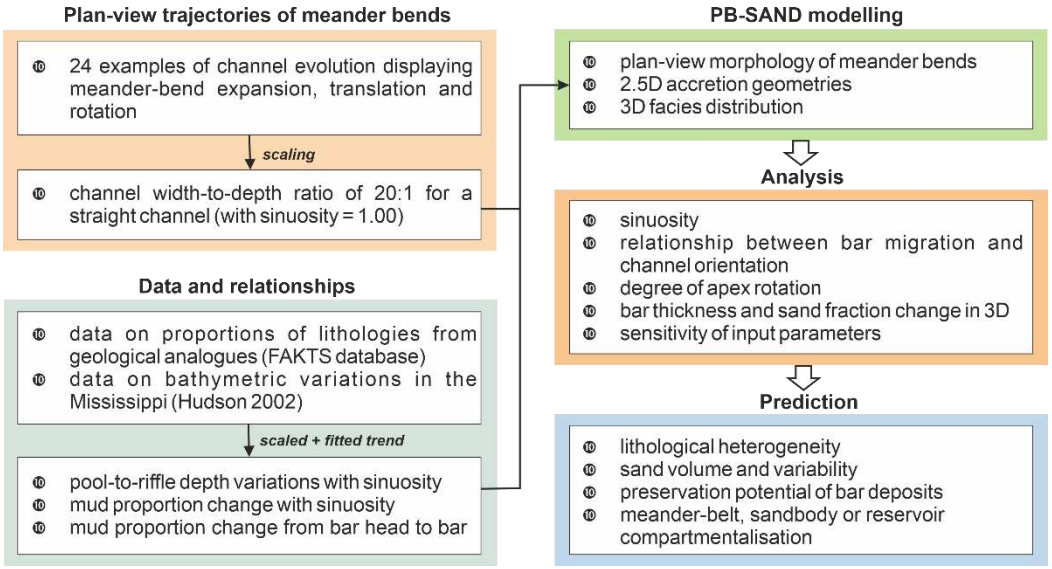

Fig. 1. Workflow for modelling sand distribution in point-bar deposits using PB-SAND, as informed by established geological knowledge, time-lapse channel trajectories derived by remote-sensing datasets, and sedimentological data from fluvial successions.

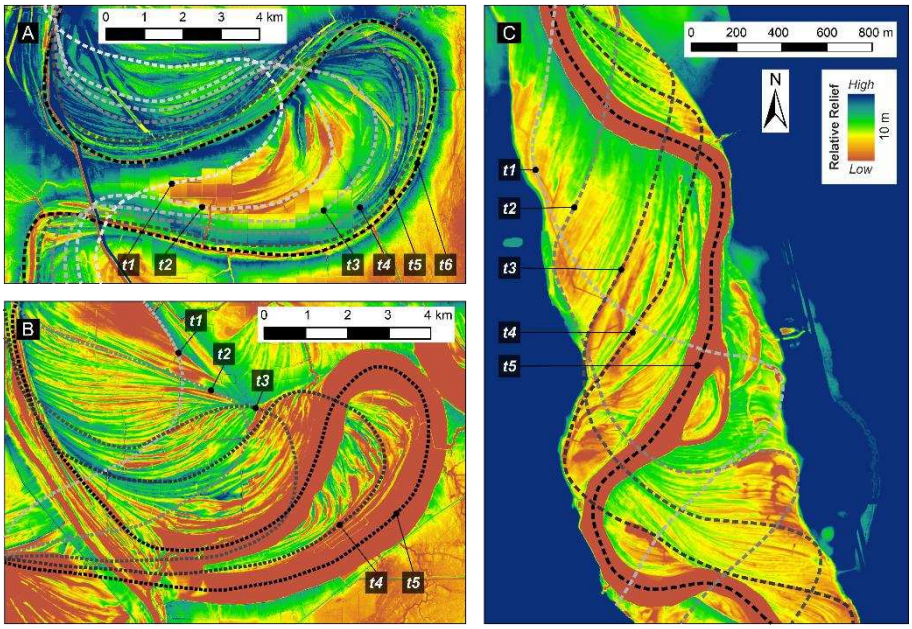

Fig. 2. LiDAR topographies illustrating examples of meander-belt segments exhibiting a combination of different transformation styles (bend expansion, translation, and rotation). For each example, centrelines tracking the position of the river channel through time are shown; these are employed as inputs to reconstruct point-bar planform evolution by PB-SAND; their relative chronological order is indicated by the colour of the dotted lines and labelled t_1 to t_n, with t_1 being the oldest trajectory. (A) and (B) are examples from the Mississippi River, Louisiana, USA; (C) is an example from the Okanogan River, Washington State, USA. The geographic location of these examples is reported in Table 2.

Input 2: channel thalweg bathymetric change and scaling

As a river channel increases in sinuosity after its inception, along-stream spatial variations in its maximum bankfull depth change through time, typically leading to the development of progressively deeper pools near meander apices and progressively shallower riffles centred on the meander inflection points (Tinkler, 1970; Yang, 1971; Keller & Melhorn, 1978; Bhowmik & Demissie, 1982). For modelling variations in channel bathymetry as a function of sinuosity change in evolving meanders, suitable empirical relationships quantifying scaling between sinuosity and pool- or riffle-depth change are lacking. To enable PB-SAND to simulate these variations in channel bathymetry in a reasonable manner, a statistical distribution of relative depth change across successive pools and riffles was considered that is based on empirical data from the lower Mississippi River (Fig. 3A; Hudson, 2002). Scaling between channel sinuosity and relative depth change was therefore established assuming: (i) straight channels to have uniform thalweg depth, and (ii) percentiles (mean, p5, p95) of distributions in the sinuosity of the modelled centrelines and descriptive statistics of relative change in channel depth (mean, minimum, maximum) to scale with each other (i.e., by linking the 5^{th} centile of sinuosity with the minimum value of depth change, etc.; Fig. 3B, C and Fig. S1). On this basis, in PB-SAND, logarithmic scaling is considered between channel sinuosity and both pool-depth increase and riffle-depth decrease.

The simulations have all been scaled on the assumptions that the channel width is the same across all models and that straight reaches take a width-to-depth ratio of 20:1 (*cf.* Whiting & Dietrich, 1993; Konsoer *et al.*, 2013), where the depth is expressed as maximum bankfull depth.

Even though channel aggradation could be modelled with PB-SAND (Yan *et al.*, 2020), in this study all simulations have been run with no net aggradation to enable isolation of the effects of planform controls on sand thickness.

Input 3: facies proportions and trends

The meander-belt deposits are modelled as being composed of two fundamental lithofacies (sand and mud) in variable proportions. Case-specific lithological data for the channel belts in the considered planform examples were not used for constraining the models, nor for scopes of validation, since the models are idealised and scale-free (i.e., are not intended to mimic specific natural examples). Instead, inputs that describe their internal lithological organisation are chosen to match with what can be considered typical in sandy meandering river systems and with consideration of common spatial trends in facies distributions. General lithological data from geological analogues were considered for constraining the models. Fig. 4A shows distributions in the proportion of mud in point-bar and counter-point-bar deposits, obtained for 6,558 facies units in 134 architectural elements from known fluvial meandering river systems stored in FAKTS (Colombera *et al.*, 2012a; Colombera & Mountney, 2019). To the best of the authors' knowledge, suitable empirical relationships that describe the variation in facies proportions in barform accretion packages as a function of sinuosity, and that could be used to inform the models, do not exist. To consider variations in the relative proportion of sand and mud in barform deposits arising from changes in formative-channel sinuosity, which would enable for example the reproduction of fining-outward trends in point bars associated with meander expansion, two sets of linear relationships between mud proportion in accretion packages of point bars and counter-point bars and associated channel sinuosity were established (Fig. 4B, C), in a manner whereby the global proportions of mud in all modelled point-bar and counter-point-bar deposits matched with median values for the FAKTS geological analogues (Fig. 4A).

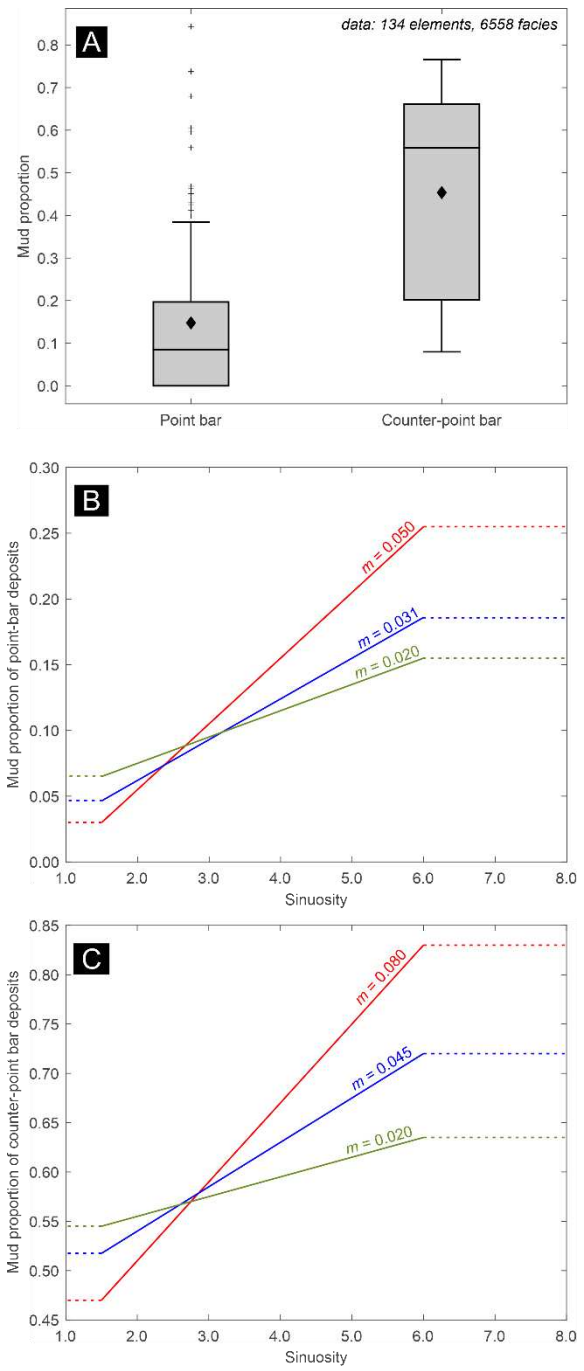

Fig. 3. (A) Data of thalweg elevation change in the Mississippi downstream of Cairo, Illinois, by Hudson (2002). Scaling relationships of pool depth increase (B) and riffle depth decrease (C), expressed relative to the depth of a straight channel, have been established by fitting logarithmic curves to percentiles (mean, p5, p95) of distributions in sinuosity in the modelled planforms and descriptive statistics (mean, minimum, maximum) of relative change of channel depth for the reach of the Mississippi River considered in (A). Distributions of pool-and-riffle differences and channel-centreline sinuosity are reported in Supplementary Fig. S1.

For simplicity, the proportion of mud in accretion packages of point-bar and counter-point-bar deposits takes a constant minimum value when the sinuosity of the channel at time of deposition is below 1.5, and a constant maximum value for sinuosity above 6.0. Three scenarios of facies trends are considered, representing different rates of change (referred to as ‘high’, ‘medium’ and ‘low’; Fig. 4B, C). Furthermore, three additional facies trends are incorporated in the model for barform deposits: (i) a fining-upward trend that culminates in mud-prone bar tops; (ii) downstream fining beyond the preserved expression of the meander apex, prescribed as a linear streamwise increase in mud proportion from the point-bar apex to the inflection point of the meander (Table 1); and (iii) progressive transition from point-bar to counter-point-bar deposits, prescribed as a linear streamwise increase in mud proportion over a transition zone centred on the inflection point of the meander and set to have a streamwise width equal to approximately three times the channel width (based on findings by Durkin *et al.*, 2019). Variations in the proportions of sand and mud across accretion packages were also

simulated stochastically (Yan *et al.*, 2017). Channel-fill deposits are also modelled, but their internal lithological make up is not considered in this work. An overview of input facies proportions is shown in Table 1, for the three scenarios of mud-fraction increase with sinuosity.

Table 1. Input facies proportions for three scenarios of rate of change in mud fraction in relation to sinuosity; facies proportions take the reported values for channel sinuosity below 1.5 and above 6.0 and vary linearly for any sinuosity value in between these two.

	Sinuosity	High rate		Medium rate		Low rate	
		Mud	Sand	Mud	Sand	Mud	Sand
Point-bar meander-apex deposits	<1.5	0.030	0.970	0.047	0.953	0.065	0.935
	>6.0	0.255	0.745	0.186	0.814	0.155	0.845
Point-bar meander-inflection deposits	<1.5	0.250	0.750	0.283	0.717	0.305	0.695
	>6.0	0.543	0.457	0.453	0.547	0.395	0.605
Counter-point-bar deposits	<1.5	0.470	0.530	0.518	0.482	0.545	0.455
	>6.0	0.830	0.170	0.720	0.280	0.635	0.365

Quantification of point-bar planform evolution and meander transformations

The planform shape of each channel trajectory (i.e., each time step of channel evolution, including both digitised input centrelines and trajectories resulting from their interpolation to define accretion increments) is determined by a predefined number of evenly spaced control points (Fig. 5; Yan *et al.*, 2017). For each simulation, the migration direction of the river channel is approximated by the direction of shift of corresponding control points across two consecutive centrelines (Fig. 5). The orientation of the channel at any one point along its course is also calculated, as a downstream-oriented vector connecting two consecutive control points along each trajectory (Fig. 5). A quantity termed 'migration angle' can therefore be obtained as the absolute angle (θ_{mig}, domain: 0°–180°) between the direction of channel migration and the circular mean of downstream channel direction; the circular mean of the channel direction serves as an approximation of the channel-belt orientation, and is used to enable discrimination of planform transformation styles.

The degree of rotation of each meander between consecutive time steps is calculated based on the change in the direction of the curve tracking the position of the meander apex, identified as the point of local maximum curvature around each bend (Fig. 5). This quantity is termed 'rotation' hereafter.

The sinuous path of each centreline is characterised in terms of: (i) its sinuosity parameter, i.e. the ratio between its streamwise length and the straight distance between centreline end points ('sinuosity' hereafter), and (ii) the circular variance of channel orientation, extracted as explained above.

Furthermore, the amount of preservation of bar deposits during the modelled channel-belt histories was calculated as the fraction of accumulated point-bar surface that has not been eroded by the migrating channel. This quantity is termed 'preservation ratio' hereafter.

To group the twenty-four simulations on the basis of characteristics of planform evolution, agglomerative hierarchical clustering based on Ward's method of minimum variance and squared Euclidean distance (Ward, 1963) was applied to data of channel migration angle, bend-apex rotation, mean sinuosity, standard deviation of channel-orientation circular variance, and preservation ratio, as determined for all channel centrelines in each example. These quantities were selected based on their expected relationships with styles of planform change.

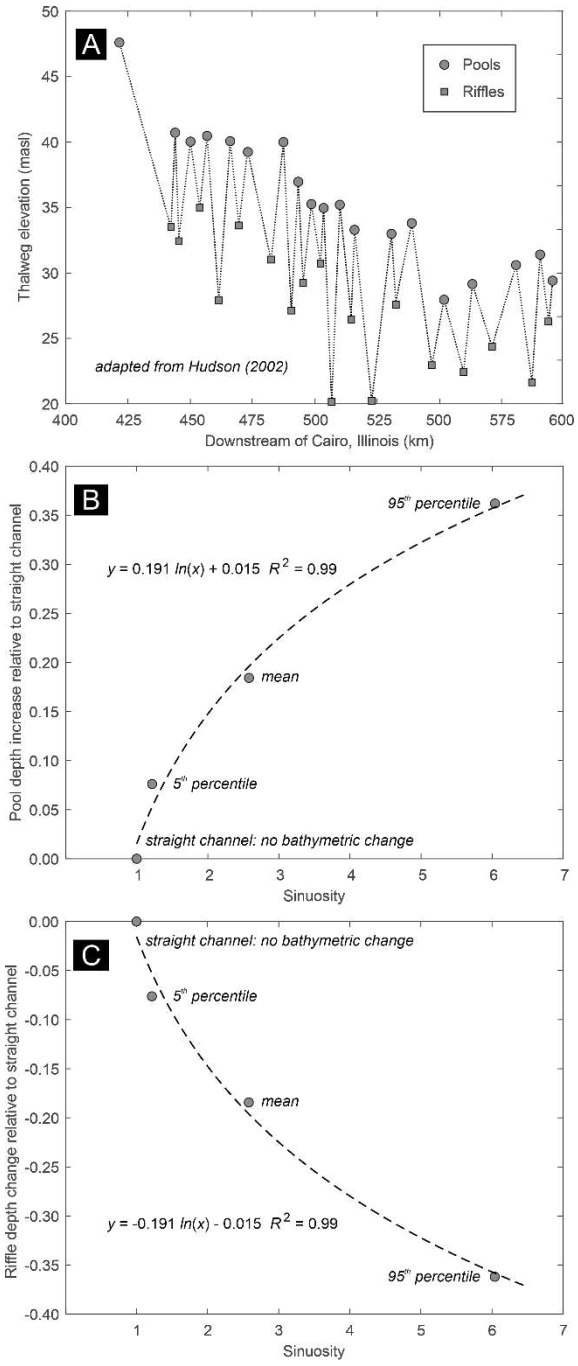

Fig. 4. (A) Distributions of mud proportion in point-bar and counter-point-bar deposits from 134 architectural elements of fluvial meandering river systems stored in the FAKTS database (Colombera *et al.*, 2012a). The bottom and top of a box denote the first and third quartiles; the horizontal black line in the box denotes the median; the whiskers on both sides extend to the minimum and maximum values excluding outliers (outside of 1.5 interquartile range); and the black diamond denotes the mean value. Based on data in (A) and sinuosity values of the employed channel centrelines (see Supplementary Fig. S1), two sets of linear relationships between channel sinuosity and mud proportion in accretion packages of point bars (B) and counter-point bars (C) were established through a trial-and-error process in a manner whereby the global proportions of mud in all modelled point-bar and counter-point-bar deposits matched with the median values of their respective distributions. Three scenarios of facies trends representing different rates of change are modelled, with high, medium and low rates shown as red, blue and green dashed lines, respectively. *m* denotes the slope of each line.

Gridding and quantification of sedimentary architectures

For each planform morphology, PB-SAND can generate lithological models that can be rendered on sets of 2D cross sections of any spacing and orientation. In this work, sets of cross sections with spacing equal to a quarter of the channel width are generated, wherein each cross section has a vertical resolution of 0.01 channel width. These sections have been used to generate 3D grids with a horizontal resolution of 0.25 channel width. Based on these grids, raster maps of sand thickness, bar thickness, and sand fraction are generated for all 72 simulations (i.e., for the combination of 24 planform cases and 3 facies trends).

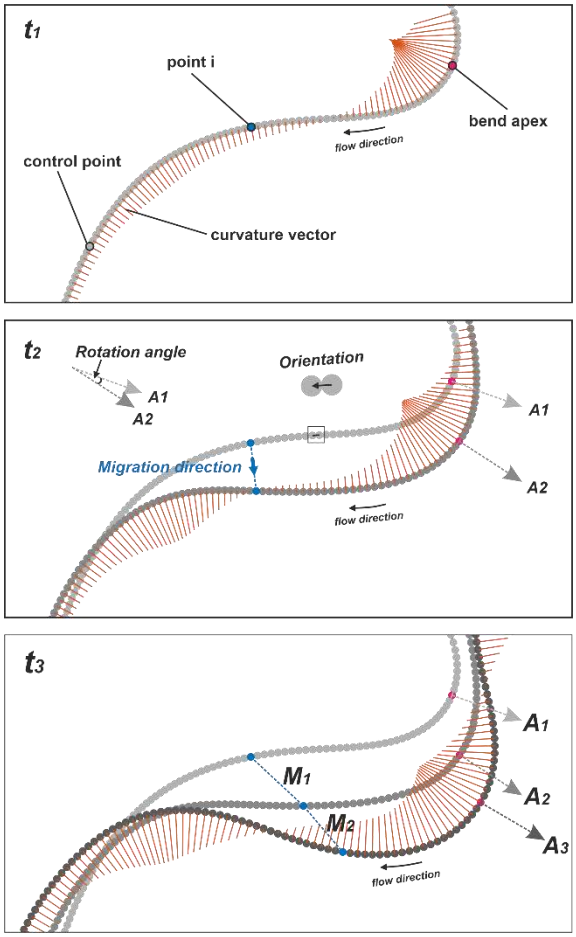

Fig. 5. Schematic diagram showing how quantitative parameters of point-bar planform evolution are defined. Control points of two consecutive channel centrelines at t_1 and t_2 are shown by the grey spots. Each centreline has the same number of control points. The migration direction is calculated by the shift of each control point across consecutive centrelines. The channel orientation is estimated as a downstream-oriented vector connecting two consecutive control points along each centreline. The red lines denote the curvature vector of each control point, and a greater length means a sharper bend. The degree of meander rotation is the angle portrayed by lines orthogonal to two consecutive centrelines at the position of local maximum curvature.

RESULTS

Planform morphology and evolution

The modelled planform morphologies of the twenty-four cases along with LiDAR images of the comparable natural examples are shown in Fig. 6. The simulations are labelled *PB1* to *PB24* in order of increasing mean value of migration angle θ_{mig} (as averaged for all time steps). The coordinates of all point-bar examples are summarised in Table 2.

The mean sinuosity of input trajectories in each case range between 1.23 and 4.74; the average is 2.43 (see Fig. 7 for z-scores). Across all time steps in each simulations, the circular variance of channel direction takes mean values ranging between 0.15 and 0.81 and standard deviation ranging between 0.02 and 0.24 (see Fig. 7 for z-scores); the arithmetic mean of channel-direction circular variance acts as proxy for channel sinuosity (displaying a Pearson's correlation coefficient of 0.90 with the sinuosity parameter), whereas its standard deviation quantifies the magnitude of temporal variation in sinuosity throughout the modelled channel-belt histories. Statistics on migration angle θ_{mig} based on all time steps are summarised for each case example in Fig. 7 and 8A. The mean values of migration angle for the twenty-four cases range between 33° and 144°, with an average value of 74°. Statistics on bend-apex rotation based on all time steps are reported for each case example in Fig. 7 and 7B-C. Mean values of apex rotation range between 1.69° and 6.26°; median values range between 0.75° and 2.43° (Fig. 8B). The cumulative amount of apex rotation that has taken place throughout the entire modelled evolution of each case is presented in Fig. 8C; however, this quantity depends on the total amount of channel migration (i.e., is a function of the rate at which, and of the time over which, the river reaches have evolved), which differs across the twenty-four examples. The preservation ratio of point-bar surfaces ranges between 0.78 and 0.98, with a mean value of 0.93 (see Fig. 7 for z-scores).

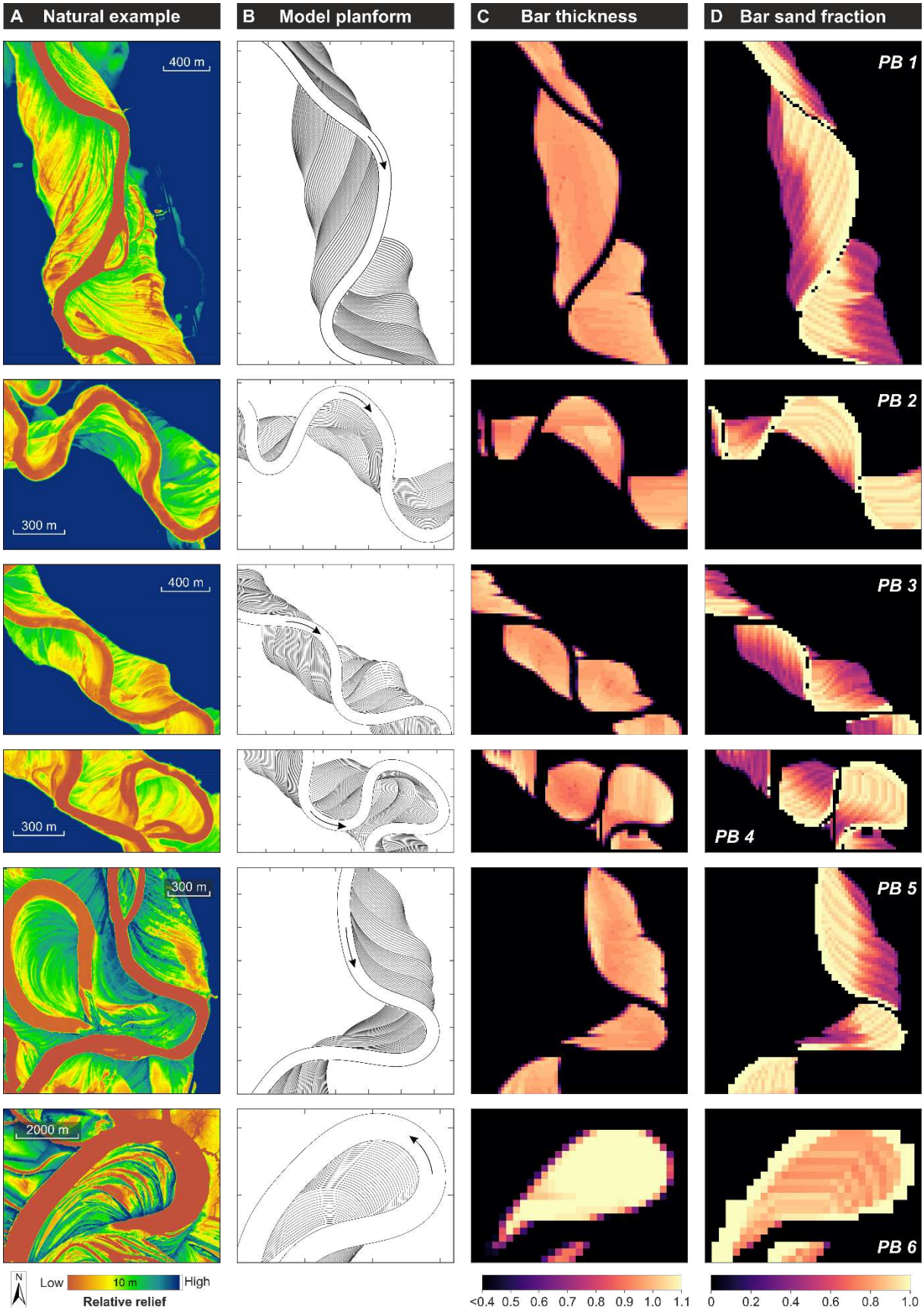

Fig. 6. (continues on the next page).

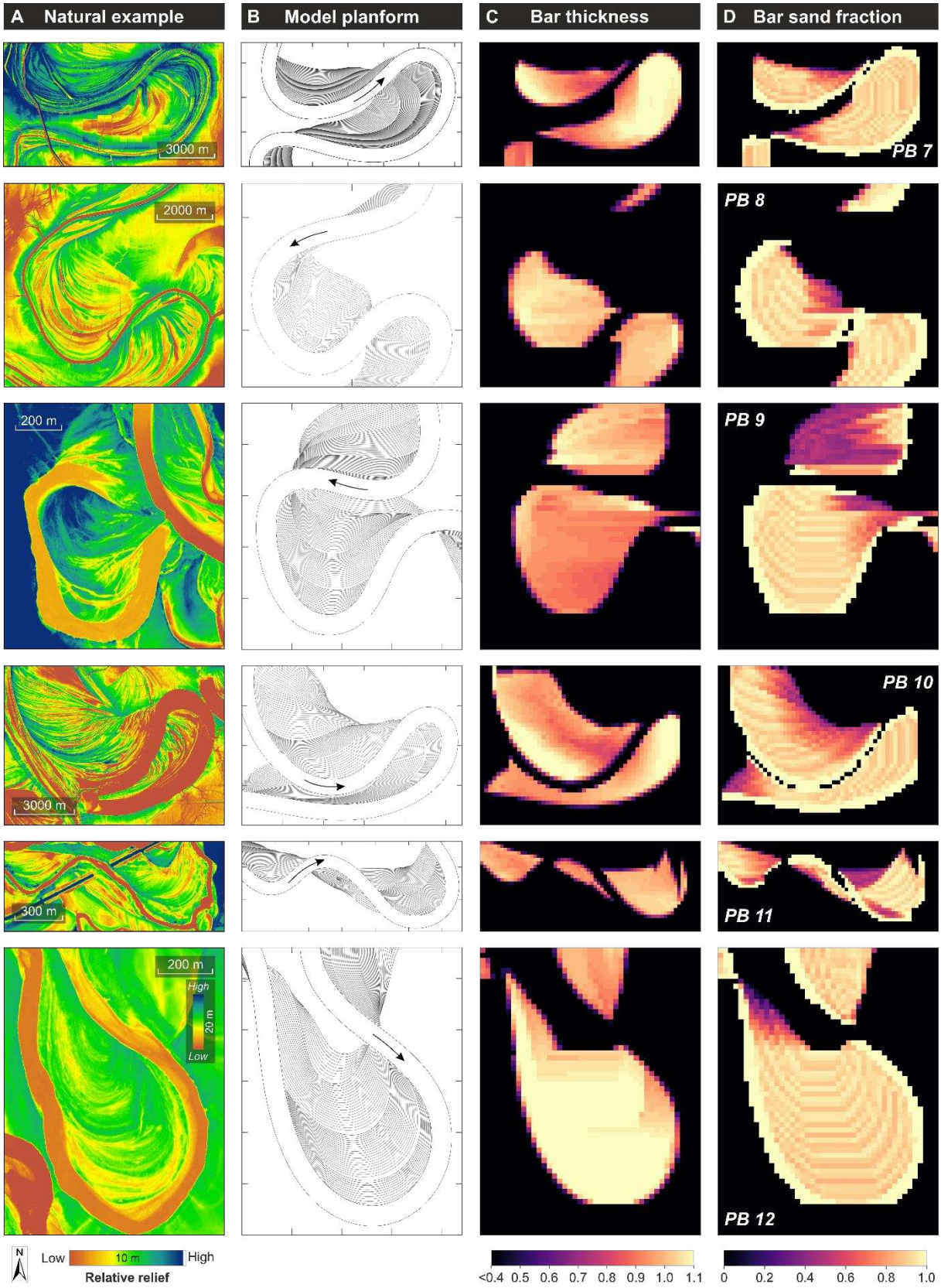

Fig. 6. (continues on the next page).

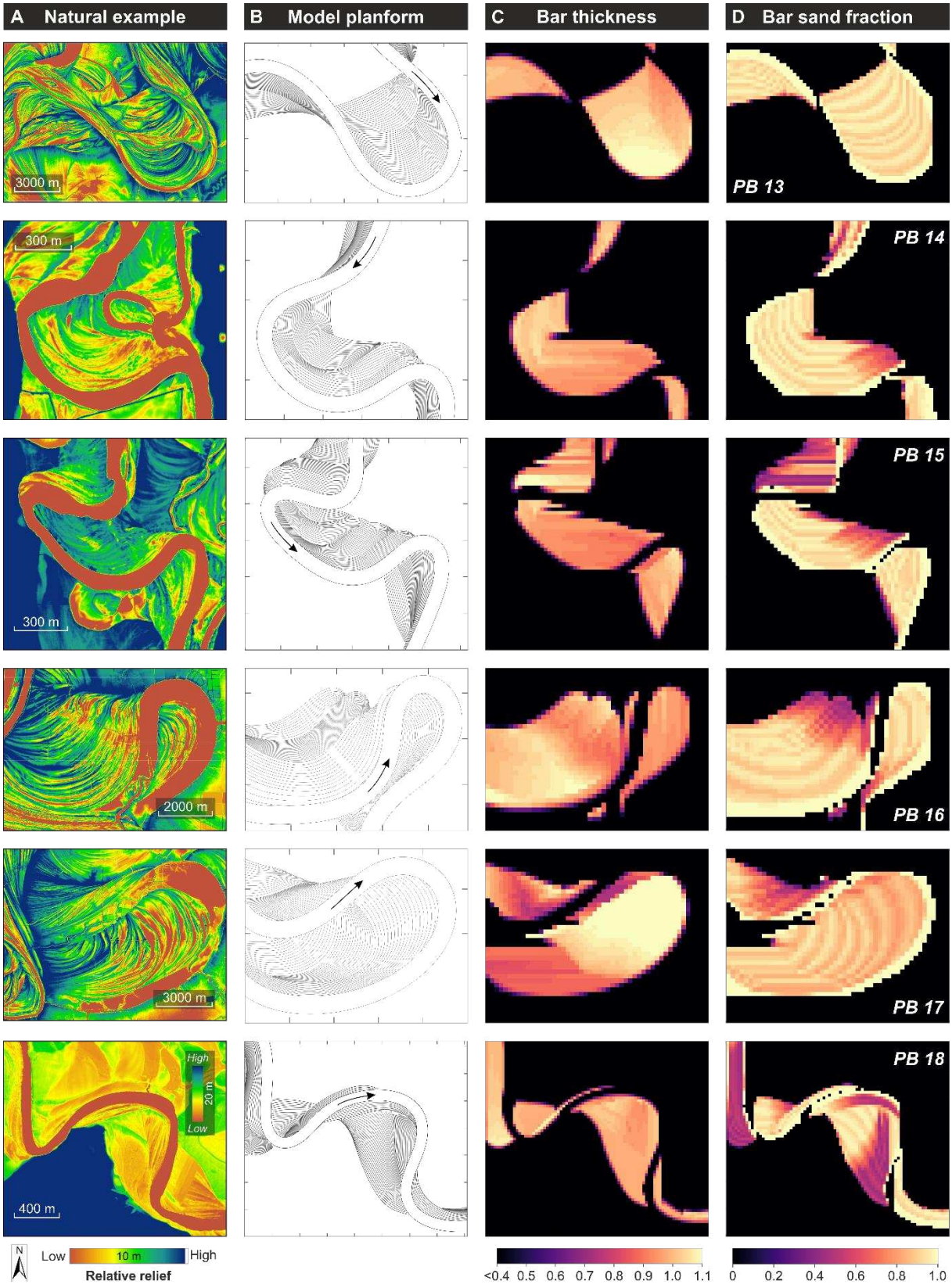

Fig. 6. (continues on the next page).

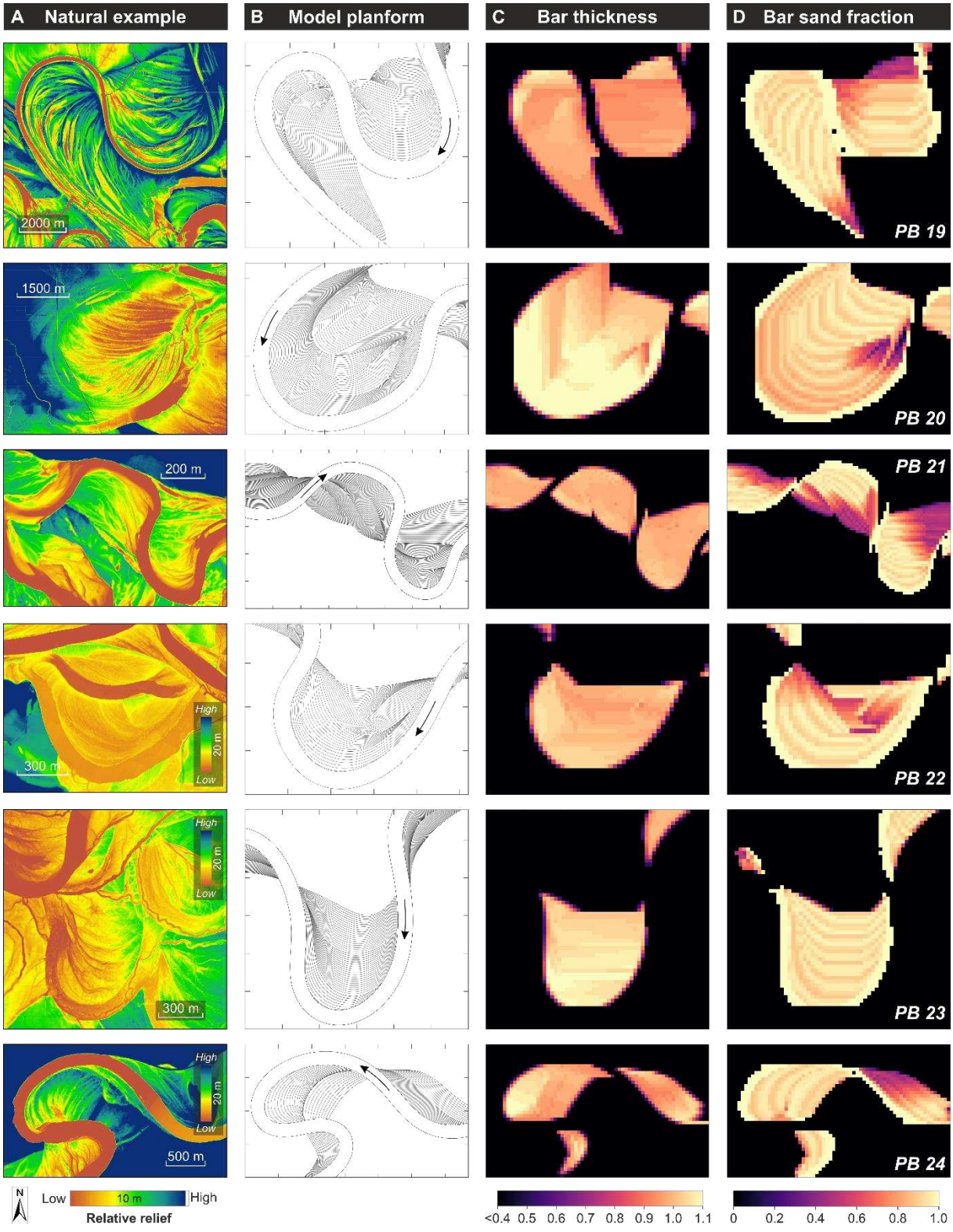

Fig. 6. Twenty-four meander belts displaying the planforms modelled using PB-SAND and corresponding model outputs (*PB1* to *PB24*). (A) high-resolution LiDAR images used to extract channel centrelines tracking the river temporal evolution, for input to PB-SAND. (B) Planform morphologies outputted by PB-SAND through linear interpolation of the input centrelines. (C) Raster maps of the thickness of bar deposits of PB-SAND geocellular outputs. (D) Raster maps of the sand fraction of bar deposits of PB-SAND geocellular outputs. Physical scales in part A do not apply to parts B-D, since all simulations have been scaled so as to have the same channel width. Some of the natural river examples contain superimposed landforms that have not been incorporated into the models because they are not the target of this study; for example: (i) the *PB4* model depicts

a time immediately prior to neck cut-off of the prominent meander loop; (ii) the *PB5* model does not incorporate the prominent meander loop developed in the west or the chute channel in the north of the natural example; the *PB9* model does not incorporate a younger low-sinuosity channel reach that has partly overprinted the earlier meander loops considered in the study; the *PB14* model does not incorporate the chute channel with a minor oxbow lake that is partly overprinting the main meander loop; the *PB22* model does not incorporate the chute channel; the *PB23* and *PB24* models do not incorporate the crevasse channels.

The results of hierarchical clustering of the twenty-four simulations – based on their migration angle, apex rotation, mean sinuosity, standard deviation of channel circular variance, and preservation ratio – are summarised as a dendrogram in Fig. 7. Three high-level clusters are considered here for further analysis, and these are termed groups 1 to 3 hereafter. These three groups display the following general characteristics:

- Group 1 (N = 5; Fig. 7) simulations are characterised by lower-than-average mean values of sinuosity (group average of 1.53), migration angle (group average of 41.6°), and standard deviation of channel-direction circular variance (group average of 0.05). The preservation ratio is lower than average for the entire cluster (group average of 0.90) and in all simulations except *PB2*.
- Group 2 (N = 12; Fig. 7) simulations are characterised by higher-than average mean sinuosity (except *PB8*, *PB21*, *PB23* and *PB24*; group average of 3.15) and/or preservation ratio (except *PB10*; group average of 0.96), and by lower-than-average mean bend-apex rotation (except *PB9*; group average of 2.39°). The mean migration angle takes a minimum value of 53.0°, a maximum of 144.4° and an average of 81.5°.
- Group 3 (N = 7; Fig. 7) simulations are characterised by lower-than-average mean sinuosity (except *PB16*; group average of 1.82) and/or preservation ratio (except *PB19*; group average of 0.88), and by higher-than-average mean bend-apex rotation (group average of 4.66°). The mean migration angle takes a minimum value of 73.0°, a maximum of 106.4° and an average of 84.0°.

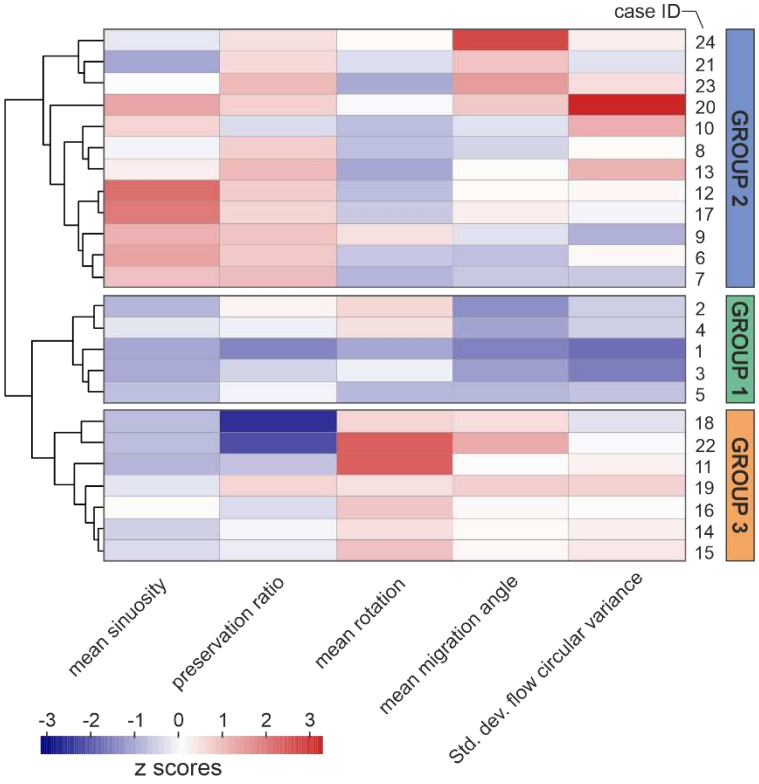

Fig. 7. Heatmap showing z-scores of the mean sinuosity, the preservation ratio, the mean rotation, the mean migration angle, and the standard deviation of circular variance in channel direction for the 24 model outputs. Results of hierarchical cluster analysis are represented as a dendrogram on the left-hand side, and the three highest-level clusters are shown on the right-hand side (groups 1, 2 and 3).

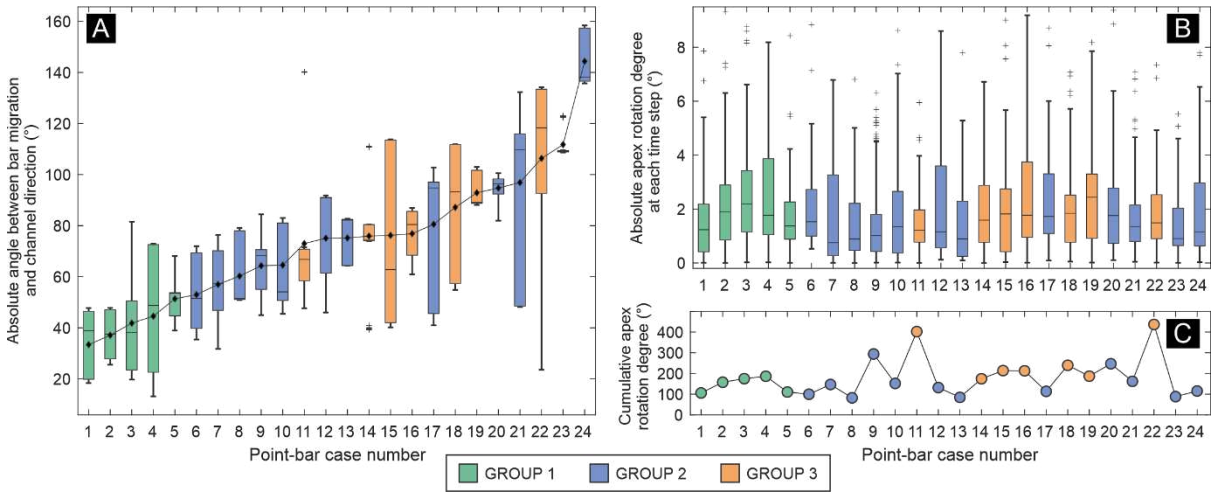

Fig. 8. (A) Distributions of the absolute angle (0° - 180°) between the direction of channel migration and the circular mean of downstream channel direction at each time step, for all case examples, summarised in order of mean values. (B) Distributions in the absolute rotation of meander apices between consecutive time steps, calculated based on the change in direction of the point of local maximum curvature around each bend, for all case examples. (C) Cumulative amount of apex rotation over time for all case examples.

Overall, the characteristics observed in group 1 are expected in channel belts in which the meander bends migrate through translation (Daniel, 1971), i.e. by downstream sweep, since this mechanism drives accretion in a direction parallel to the channel-belt axis and in a manner whereby channel sinuosity tends to be maintained through time. This process is also conducive to point-bar cannibalization, although the degree to which this is recorded in the preservation ratio is necessarily also a function of the magnitude of channel migration, and so of the length of time and migration rates being modelled (*cf.* Ielpi and Lapôtre, 2020). This inference is in accord with a qualitative evaluation of channel-belt accretion geometries (see Figs 5 and 6). Therefore, in subsequent analyses, this group of simulations will be considered as representative of channel belts dominated by meander-bend translation.

Some of the characteristics observed in groups 2 and 3 are compatible with what can be anticipated for channel belts in which the dominant style of meander transformation is by bend expansion (Daniel, 1971), since this process results in point-bar growth at high angle to the channel-belt axis and drives temporal increases in channel sinuosity. Although this may not be evident based on the planform geometry of the last active channel, or from an evaluation of preserved channel-belt accretion geometries (Fig. 7), overall variations in mean bend-apex rotation and preservation ratio across groups 2 and 3 are attributable to an increased prevalence in group-3 examples of meander-bend rotation (Daniel, 1971) as a primary agent of planform change and point-bar erosion. Therefore, in subsequent analyses, simulations in groups 2 and 3 are both considered as representative of channel belts dominated by meander-bend expansion, but respectively experiencing relatively lower or higher degrees of bend rotation.

These fundamental differences across the three groups will be used to relate stratigraphic products to dominant style of planform change. Notwithstanding, a qualitative visual analysis of the planform evolution of the modelled channel belts reveals that combination of different modes of meander-bend transformation – across different bends in the same reach and through the temporal evolution of each meander – is the norm (Fig. 7).

Across the twenty-four simulations, the preservation ratio displays moderate positive correlation with mean sinuosity (Pearson's $R = 0.56$, $p = 0.005$; Fig. 7) and moderate negative correlation with mean rotation ($R = -0.52$, $p = 0.009$; Fig. 7); this is likely a record of the

erosional effects of processes of meander-bend translation and rotation. A modest negative relationship is seen between mean sinuosity and mean rotation (R = -0.39, p = 0.058; Fig. 7).

Table 2. Coordinates of 24 meander belts whose topography is shown in high-resolution LiDAR images used to define PB-SAND input centrelines.

Point-bar Number	Coordinates		Location
1	119° 24' 56" W	48° 50' 00" N	Okanogan, USA
2	29° 28' 07" E	66° 20' 37" N	Oulanka, Finland
3	29° 33' 21" E	66° 18' 45" N	Oulanka, Finland
4	29° 30' 36" E	66° 19' 54" N	Oulanka, Finland
5	119° 25' 11" W	48° 51' 31" N	Okanogan, USA
6	91° 32' 36" W	31° 53' 57" N	Mississippi, USA
7	91° 53' 16" W	30° 48' 53" N	Mississippi, USA
8	91° 21' 29" W	32° 18' 37" N	Mississippi, USA
9	119° 42' 43" W	48° 57' 43" N	Okanogan, USA
10	91° 32' 18" W	31° 46' 13" N	Mississippi, USA
11	119° 39' 24" W	48° 55' 40" N	Okanogan, USA
12	120° 06' 00" W	46° 15' 34" N	Yakima, USA
13	91° 27' 19" W	31° 51' 10" N	Mississippi, USA
14	119° 26' 11" W	48° 53' 35" N	Okanogan, USA
15	119° 26' 15" W	48° 54' 30" N	Okanogan, USA
16	91° 44' 45" W	31° 29' 31" N	Mississippi, USA
17	91° 38' 19" W	31° 38' 40" N	Mississippi, USA
18	120° 03' 53" W	46° 14' 42" N	Yakima, USA
19	91° 21' 50" W	32° 03' 30" N	Mississippi, USA
20	92° 02' 39" W	30° 55' 20" N	Mississippi, USA
21	119° 40' 28" W	48° 56' 47" N	Okanogan, USA
22	120° 01' 21" W	46° 13' 56" N	Yakima, USA
23	121° 34' 19" W	48° 28' 42" N	Skagit, USA
24	121° 50' 24" W	48° 32' 05" N	Skagit, USA

Meander-belt architectures

The internal architecture of the modelled channel belts can be characterised in terms of (i) relative fraction of point-bar and channel-fill deposits, (ii) overall sand proportion in point-bar elements, (iii) spatial variability in the thickness of point-bar deposits, and spatial variability in the (iv) thickness and (v) proportion of sand in point-bar elements. The spatial variability of sand thickness and proportion can be represented in raster maps with resolution of a quarter of channel width (Fig. 6). The spatial distribution of sand in point-bar deposits varies across the three sets of simulations associated with the three scenarios of facies trends, each representing a different rate of change of sand proportion in point-bar accretion packages with channel sinuosity. The planform distribution of sand thickness and fraction in point-bar deposits is presented for the intermediate facies trend (Fig. 6), for the trend representing low rate of change (Fig. 9A and C), and is in addition expressed as relative variation between the low and high trends (Fig. 9B and D).

At any one location in the model domains, the thickness of point-bar deposits reflects both the direction of shift of pool and riffle zones and their degree of bathymetric differentiation as the channel sinuosity changes through time. As expected, this results in

downstream-elongated zones of maximum and minimum point-bar thickness in reaches dominated by meander translation (e.g., *PB1*), and in a progressive increase in point-bar thickness towards the cut-bank in pool areas of reaches dominated by meander expansion (e.g., *PB13*). Spatial variability in point-bar thickness additionally arises where sets of lateral-accretion packages are juxtaposed laterally, in contact with each other through erosional surfaces (e.g., *PB22*).

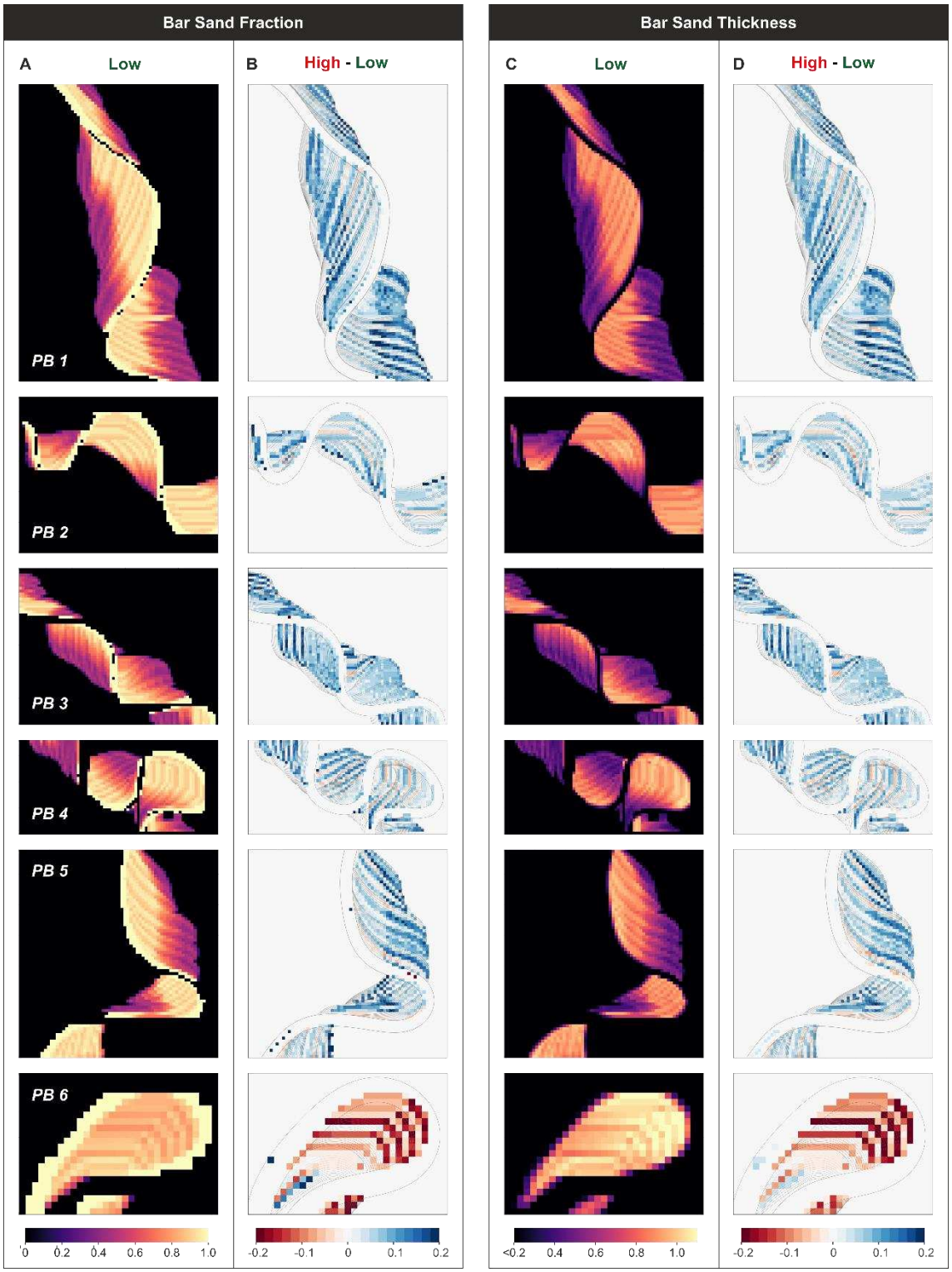

Fig. 9. (continues on the next page).

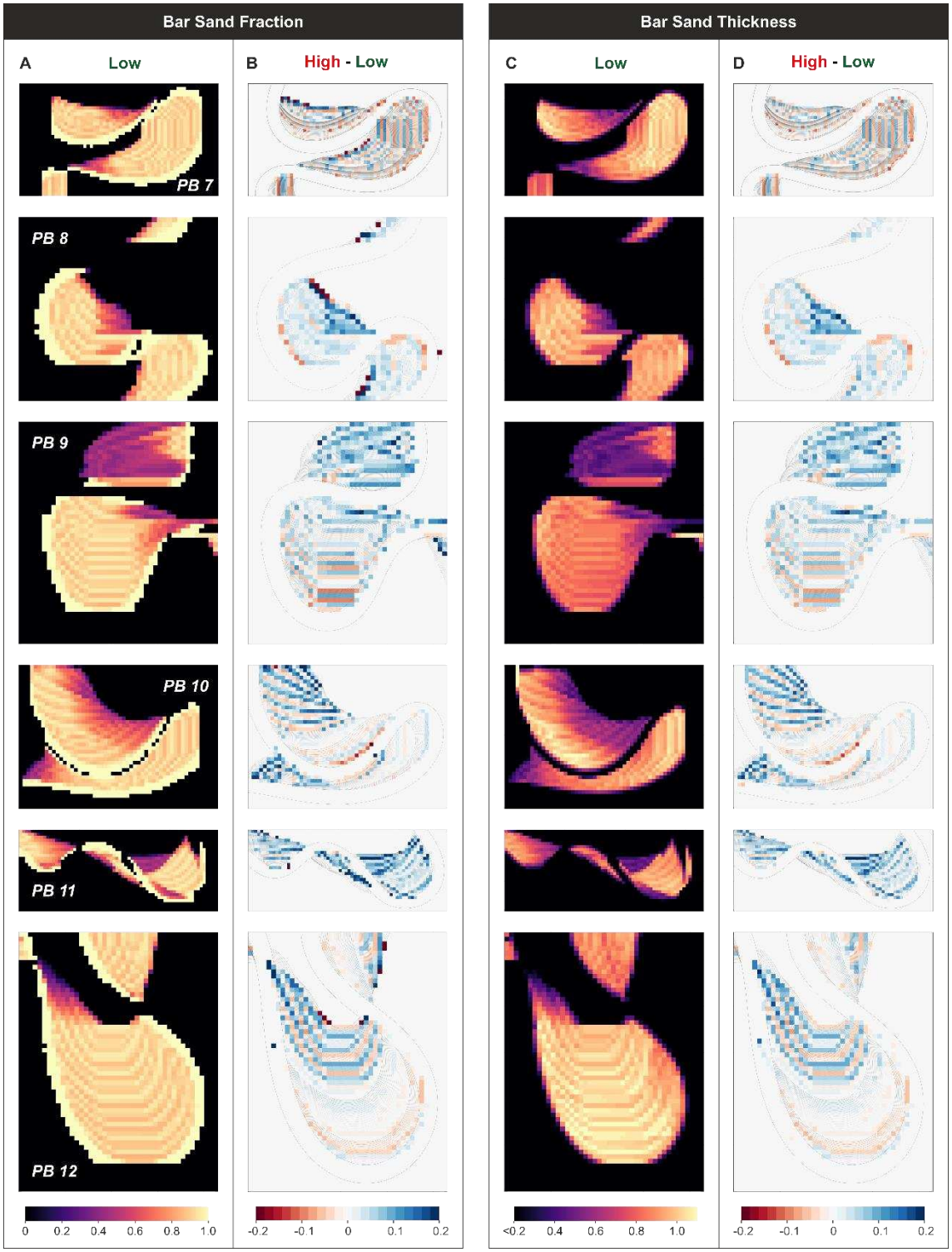

Fig. 9. (continues on the next page).

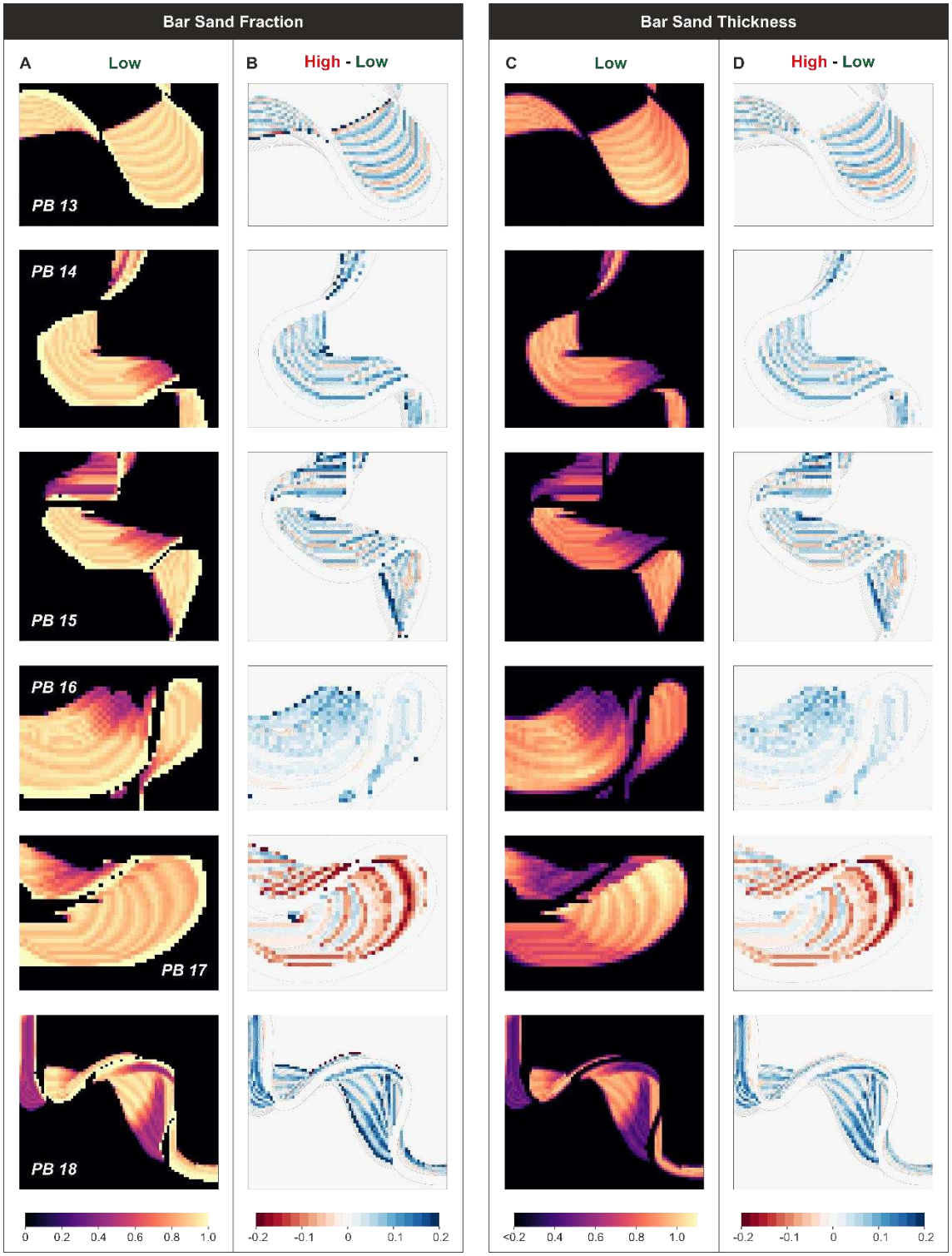

Fig. 9. (continues on the next page).

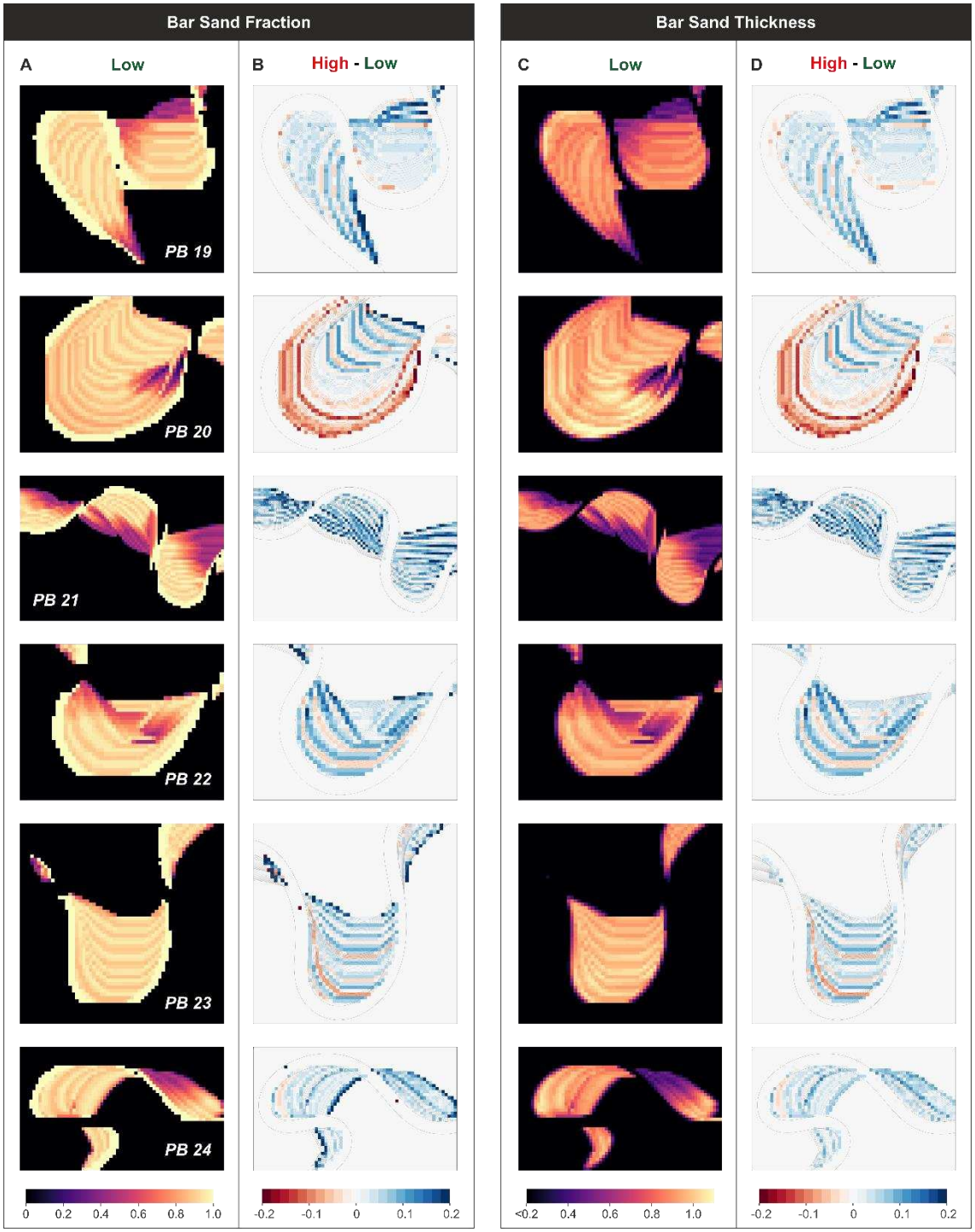

Fig. 9. Maps of sand fraction and sand thickness in point-bar deposits modelled by PB-SAND (*PB1* to *PB24*). (A) and (C) depict results for simulations associated with low rate of change in sand proportion with sinuosity. (B) and (D) depict the relative differences between the high and low rates of change in sand proportion with sinuosity. Physical scales in part A do not apply to parts B-D, since all simulations have been scaled so as to have the same channel width.

Variations in the thickness and proportion of sand in point-bar elements – both across different simulations and spatially within the model domain of each – reflect both variations in point-bar thickness and facies trends describing changes in sand deposition both in space (i.e., around a meander bend) and time (i.e., as a function of sinuosity). The imposed facies trends are present in variable magnitude. A transition from sand-prone point-bar deposits to

relatively more mud-prone counter-point bar deposits is evident in cases dominated by bend translation (e.g., *PB3*), and more generally where concave-bank accretion is preserved (e.g., *PB20*). A trend of point-bar fining downstream of the preserved expression of meander apices is more subtle, but evident in sand thickness and fraction maps of some examples that grew by bend expansion (e.g., *PB21*). A trend of reduction in point-bar sand thickness and fraction across accretion packages deposited as the formative channel became progressively more sinuous is also subtle, but recognised in examples dominated by meander expansions (e.g., *PB20*).

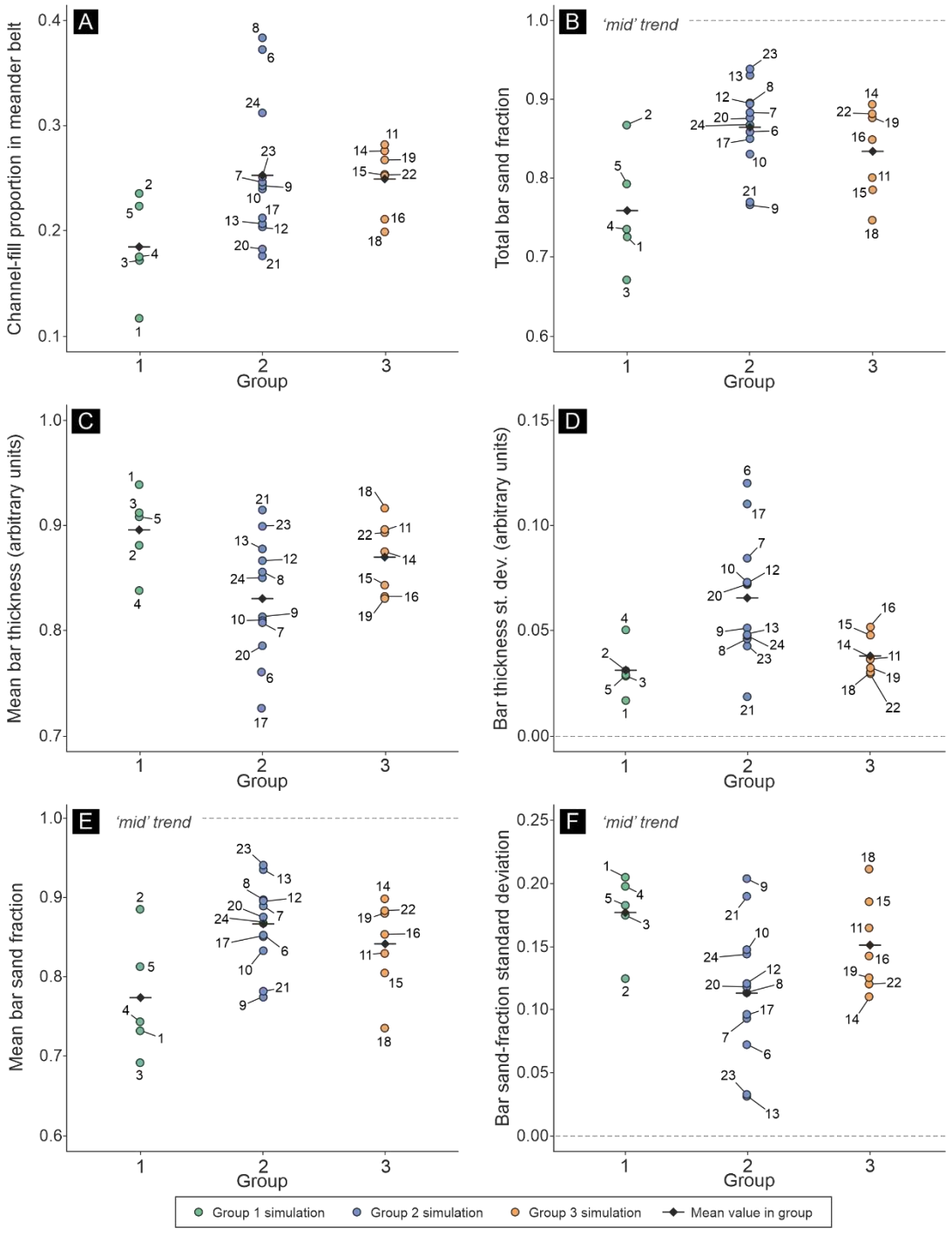

Fig. 10. (A) Channel-fill proportion in meander belt, (B) total bar sand fraction, (C) mean bar thickness, (D) Standard deviation of bar thickness, (E) mean bar sand fraction, and (F) standard deviation of bar sand fraction, of three point-bar groups classified based on the characteristics of meander planforms.

Relationships between facies heterogeneity and point-bar planform evolution

The parameters used to describe river planform changes allow evaluation of relationships between the lithological organisation of the modelled meander belts and their planform evolution. This evaluation can be undertaken by (i) considering variations in characteristics of the internal architecture of the modelled channel belts across the three high-level clusters of simulations, and by (ii) determining bivariate relationships between these characteristic and the planform parameters.

Based on maps of point-bar thickness, sand thickness and sand fraction, values of mean and standard deviation were extracted to quantify variations in these variables across the three groups, and this was done for the three sets of simulations associated with the variable trends of sand deposition as a function of sinuosity (Figs 9 & 10). The standard deviation of bar thickness is lowest, on average, for simulations from group 1, and on average lower in simulations from group 3 than in those from group 2 (Fig. 10D). This reflects variations in sinuosity across the three groups (Fig. 7), since sinuosity determines changes in thalweg depth across pools and riffles (Fig. 3B-C), and is consistent with the fact that river reaches that are dominantly undergoing meander translation experience relatively more limited changes in sinuosity, since the form of translating bends remains broadly similar through time. For the same reason, the fraction of channel-belt deposits made of channel fills is slightly larger, on average, in the meander belts of simulations from group 2 and 3, relative to those of group 1 (Fig. 10A). The overall proportion of sand in point-bar deposits varies between 67% and 94%, recorded in simulations from group 1 and 2, respectively (Fig. 10B). When local values of point-bar sand thickness and fraction are considered, there exists considerable spread in the data and important overlaps across the three groups (Figs 9E-F and 10). Notwithstanding, values of sand thickness are on average lower and more variable in point-bar deposits of simulations from group 1, even though these point-bar elements tend to be thicker and less variable in thickness (Figs 9C-D & 10A-B); this highlights the dominant control of facies trends over bathymetric changes in determining sand thickness for the chosen model inputs. Accordingly, values of local sand fraction are on average smaller and marginally more variable in simulations from group 1 relative to the other two groups, regardless of the type of facies trend used as input (Figs 9E-F & 10C-D). The interplay of facies trends and bathymetric changes, both related to channel sinuosity, gives rise to variations in both bar thickness and sand proportion that can variably control local values of sand thickness and their spatial variability. Based on the chosen inputs, in simulations from groups 1 and 3, an increase in the rate of facies change in response to variations in channel sinuosity corresponds to an overall increase in mean values of point-bar sand thickness and fraction, and to an overall decrease in their standard deviation (Fig. 11). In simulations from group 2, changes in mean and standard deviation of point-bar sand thickness and proportion in response to the strength of the facies trend are variable in sign and magnitude. The key planform and facies characteristics of the three groups resulting from the cluster analysis are summarised in Table 3.

Across all the model outputs, the spatially averaged mean values of point-bar thickness are inversely correlated with river sinuosity (Pearson's $R = 0.79$, $p < 0.001$; Fig. 12A), whereas the standard deviation of point-bar thickness demonstrates the expected positive relationship with sinuosity ($R = 0.87$, $p < 0.001$; Fig. 12B). The average sand fraction in bar deposits shows modest correlation with the average channel migration angle (Fig. 12C). The average sinuosity displays weak to moderate positive correlations with both (i) the total amount of point-bar sand as a fraction of channel-belt deposits (Fig. 12D), and (ii) the average point-bar sand fraction (Fig. 12E). The standard deviation of sand fraction in bar deposits shows instead a negative correlation with mean sinuosity (Fig. 12F). The sand fraction standard deviation is also positively correlated to the mean apex rotation, but the

correlation is weak and not statistically significant ($R = 0.33$, $p = 0.121$). The preservation ratio correlates positively with the mean sand fraction of bar deposits (Fig. 12G) and negatively with sand-fraction standard deviation (Fig. 12H).

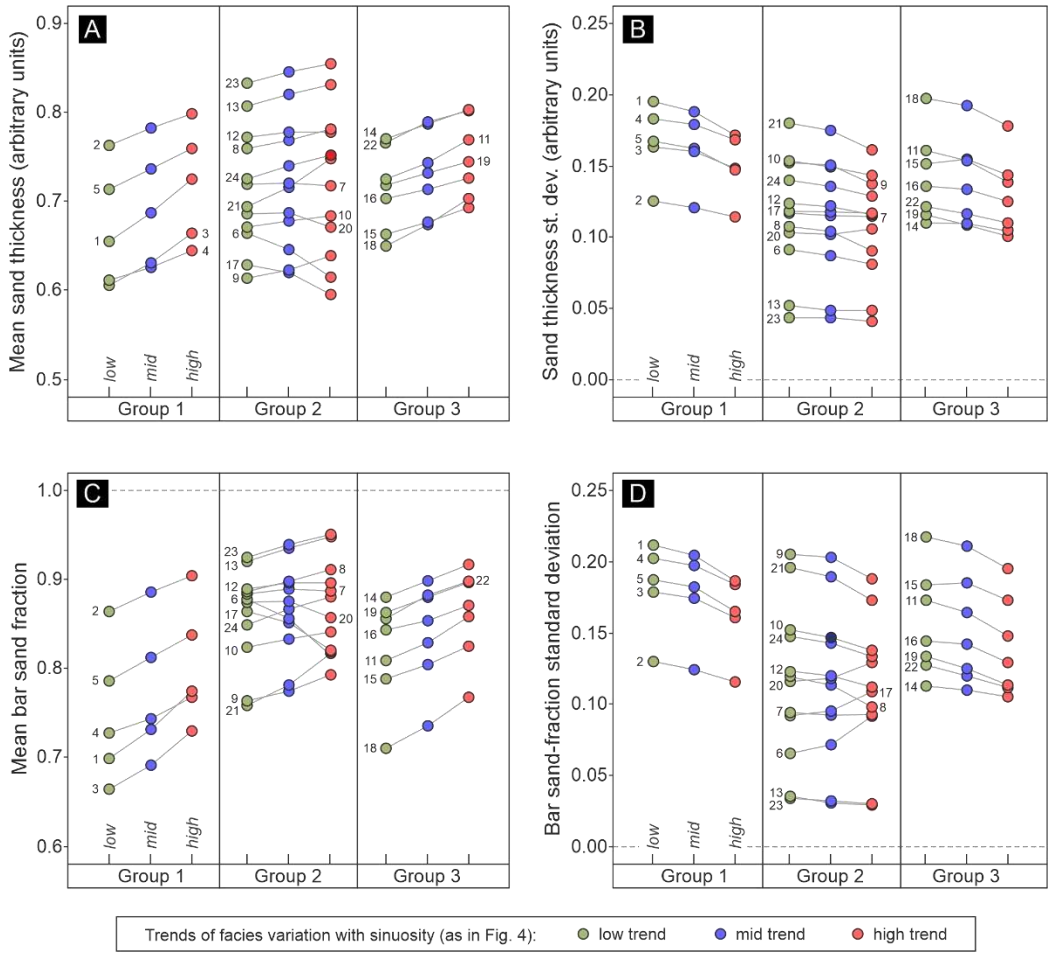

Fig. 11. (A) Mean sand thickness, (B) standard deviation of sand thickness, (C) mean bar sand fraction, and (D) standard deviations of bar sand fraction, of three point-bar groups with three different rates of change in facies trends.

DISCUSSION

Summary

The internal architecture of point-bar elements is the product of channel migration and planform change, taking place according to different styles of meander transformation that can alternate in time through different stages of bar development (Finotello *et al.*, 2020; Ghinassi *et al.*, 2016; Ghinassi *et al.*, 2014; Jackson, 1976; Miall, 1996; Schwenk *et al.*, 2017; Strick *et al.*, 2018). Because of relationships between meander morphodynamics and river hydrodynamics, the sinuosity of meanders and the accretion geometries of their associated point bars are closely related to spatial variations in facies arrangements, in bar thickness, and in the degree of preservation of bar deposits (Bridge, 2003; Ielpi & Ghinassi, 2014; Schwenk, 2016). The bathymetric difference between channel pools and riffles causes point-bar deposits to generally decrease in thickness from portions that accumulated near the meander apex to those deposited in proximity of the channel inflection point. The increase in sinuosity associated with lateral expansion of meanders amplifies the difference in depth between channel pools and riffles, causing progressive thickening – away from the initial inner bank, carved by the channel after avulsion or cut-off, and towards the outer cut bank –

of channel-belt deposits that accumulated near the pools; this trend is commonly accompanied by an overall fining-outward facies trend, related to an overall decrease in flow energy due to a decrease in streamwise channel gradient (Durkin *et al.*, 2015; Piet, 1992).

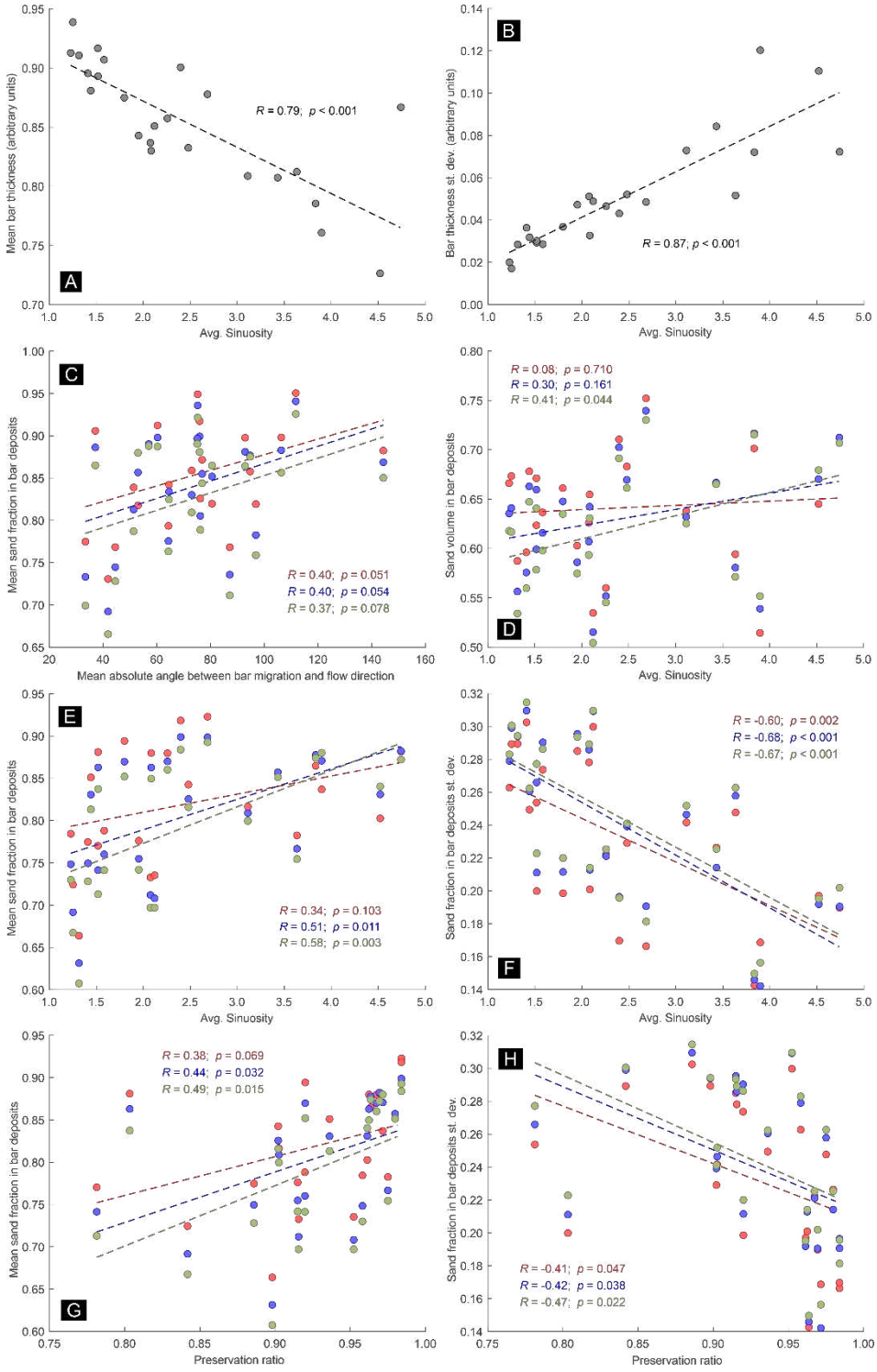

Fig. 12. Scatterplots of (A) mean bar thickness vs. average meander sinuosity, (B) standard deviation of bar thickness vs. average meander sinuosity, (C) mean sand fraction in bar deposits vs. mean absolute angle between bar migration and flow direction, (D) sand volume in bar deposits vs. average meander sinuosity, (E) mean sand fraction in bar deposits vs. average meander sinuosity, (F) standard deviation of sand fraction in bar deposits vs. average meander sinuosity, (G) mean sand fraction in bar deposits vs. preservation ratio, and (H) standard deviation of sand fraction in bar deposits vs. preservation ratio.

The downstream migration of translating meanders enables the preservation of the finer-grained deposits accreting on concave channel banks, especially where a hydraulic separation zone develops and reverse eddy currents are established, forming counter-point-bar deposits (Ghinassi *et al.*, 2016; Jackson, 1976; Makaske & Weerts, 2005; Nanson & Page, 2009; Nicoll & Hickin, 2010; Smith *et al.*, 2009; Taylor *et al.*, 1971). Rotational shifts of meander apices may also significantly rework point-bar deposits formed in the preceding stages of bar development and be recorded as erosional boundaries between sets of accretion packages (Durkin *et al.*, 2015; Johnston & Holbrook, 2019; Strick *et al.*, 2018). Therefore, the styles of meander-bend transformation, the direction, magnitude and frequency of apex rotation, and their unique sequential arrangement control the degree of preservation, facies heterogeneity, sand volume, and spatial variability thereof in point-bar deposits.

Informed by understanding of how meander morphodynamics and river hydrodynamics control the geometry and facies distributions of point-bar deposits, a set of numerical simulations has been set up in this work to explore how channel shape (sinuosity, bathymetry, type of meander transformation) and lithological trends interact to determine variability in the distribution of sand in the channel belts of sand-prone meandering river systems. A forward stratigraphic model, PB-SAND, was employed to predict 3D sand distribution of point-bar deposits associated with complex planforms and developed through multiple stages of meander transformations. The challenge in taking such an approach is to constrain the forward model in a realistic way, given that (i) quantitative relationships between planform characteristics and change in facies proportions in point-bar deposits are only known for a limited number of specific examples (e.g., Alexander, 1992; Durkin, 2016), and (ii) a compilation of quantities describing bathymetric changes as a function of river sinuosity, based on many rivers, is not yet available. A process-based, rather than geometric, modelling approach may be preferable in consideration of these issues, and a process-based modelling approach has indeed been applied to address broadly similar research questions by Willis & Tang (2010). However, employment of a geometric-oriented modelling approach has the following benefits: (i) the ability to reproduce sedimentary architectures related to complex planform changes, as seen in natural rivers, (ii) the ability to readily characterise channel planforms and changes thereof in a quantitative manner, thereby facilitating the assessment of relationships between river evolution and preserved sedimentary architectures. To generate realistic sedimentary architecture and facies distributions comparable to those observed in nature, the forward model was constrained using: (i) lithological data from a range of geological analogues; (ii) planform evolutions comparable to those of twenty-four natural river reaches, as seen in high-resolution LiDAR datasets; and (iii) variations in pool and riffle depth with river sinuosity that result in channel bathymetric changes comparable to those seen in the lower Mississippi (Hudson, 2002).

Statistical analysis of modelling outputs shows how planform evolution, channel bathymetry and facies trends interplay to affect sand volume and heterogeneity of point-bar deposits. Most of the modelled meander-belts have experienced multiple stages of bar development, through a combination of different meander-transformation styles and various magnitudes and directions of apex rotation; furthermore, the number of meander bends being considered vary both across some of the examples and, in some cases, through time in a model. All this leads to difficulties in relating planform characteristics to facies distributions; despite these difficulties, several noteworthy overall discussion points can be surmised.

Despite selecting a model set-up that forced a decrease in sand proportion in point-bar accretion packages with increasing sinuosity of the formative channel, the mean value of local sand fraction in bar deposits does not tend to decrease as the average sinuosity of meander-belt centrelines increases. This reflects how expansion-dominated point bars bear the record of channels that, through time, were on average more sinuous than translation-

dominated point bars, and how preservation of concave-bench accretion deposits in the latter type has a stronger influence on sand fraction, for the chosen model inputs and even for the strongest facies trend (Fig. 11E). Translation-dominated meander-belts are characterised by channels that tend to maintain their sinuosity by downstream migration, while simultaneously allowing the development of counter-point-bar deposits. As could be anticipated, given the model inputs (Fig. 4A), the preservation of counter-point-bar units exerts a greater impact on facies heterogeneity than temporal variations in sinuosity (Smith *et al.*, 2009; Nicoll & Hickin, 2010; Durkin *et al.*, 2015; Ghinassi *et al.*, 2016); in part, this may also be due to the models being constrained as displaying a downstream-fining trend, taking place downstream of the apices of meanders of any sinuosity and also imposed on the deposits of expansional bends, since this trend partly determines how the target facies proportions are reached (and therefore how sand and mud are distributed in space) in the model.

The prescribed trends of variations in sand proportion and channel maximum bankfull depth (i.e., bar thickness) with sinuosity interact to determine variations in local values of sand thickness. For meander-belts in which bend expansion dominates, as meander sinuosity increases, the deepening of pool zones is reflected in a local increase in bar thickness, which could potentially translate to an increase in sand thickness; this trend is however counteracted by the decrease in sand fraction caused by the fining-outwards trends. Based on the chosen model inputs, the overall increases in sand thickness seen in accretion packages deposited by highly sinuous meanders indicate that bathymetric variations exert a greater impact on sand thickness than the imposed variation of sand proportion with sinuosity (e.g., *PB13*, *PB17* and *PB20* in Fig. 9). Downstream-translating point bars are produced by channels that tend to maintain their sinuosity as bar-head deposits undergo progressive erosion by the migrating meanders, and are therefore associated with more limited spatial variability in bar thickness; because of their input facies make-up, the sand thickness is always significantly reduced in areas deposited near meander apices on concave banks. On convex banks, however, increases in pool depth act to outcompete the effects of fining-outwards trends, resulting in a tendency of increased pool-zone sand thickness in more sinuous reaches (e.g., *PB4*, *PB5* and *PB10* in Fig. 9). Changes in the rotation direction of meander apices leads to the migration of pool zones and to variable degrees of erosion of deposits accumulated in the earlier stages of bar development, especially of deposits accumulated near riffle zones. This results in the development of mosaics of juxtaposed accretion packages characterised by abrupt changes in bar and sand thickness. However, the amount of bend rotation is not associated with important spatial variability in sand volumes for the selected model inputs.

Applications

The work presented in this paper can be applied to the evaluation and ranking of different prospects in fluvial meander-belt subsurface successions that are imaged in 3D reflection seismic datasets and that host hydrocarbon reservoirs. The workflow can also be applied to subsurface characterisation more generally, for example for assessing volumes and heterogeneity of aquifers, for underground sequestration of carbon dioxide or for underground storage of hydrogen or other fluids. Two ways in which the content of this study is applicable to subsurface studies are as follows:

1) 3D geocellular models can be built using PB-SAND, as constrained by channel trajectories that reflect recognisable accretion geometries of point-bar elements and by facies and bathymetric trends, such as those employed in this work (*cf.* Colombera *et al.*, 2017, 2018, 2019). This workflow allows prediction of sand volumes and spatial distributions of point-bar sand under multiple scenarios of planform evolutions and facies trends, for purposes of uncertainty assessment.

2) Centrelines tracking the temporal evolution of the river channel, as inferred from point-bar accretion geometries observed on seismic time or stratal slices, can be digitised and quantified using the parameters considered as planform descriptors in this work; this therefore enables comparisons of the likely relative prospectivity of different reservoir sectors.

Limitations

By producing scale-free modelling outputs, the influence of physical scale on channel hydrodynamics and meander morphodynamics has been ignored. Statistics extracted from data on the lithology of point-bar deposits as seen in a range of geological analogues have been taken as representative of sand-bed rivers of any size. However, in reality, the lithology of point-bar deposits is expected to vary as a function of variables that are controlled by the scale of the river systems (e.g., influence of hydrodynamics on grainsize) or that covary with river size (e.g., influence of down-river mass extraction, sorting and comminution on grainsize). Furthermore, pool-to-riffle depth variations are modelled as a function of sinuosity based on data from a single example, the lower Mississippi from Illinois to Louisiana, and it is possible that relationships between river bathymetry and sinuosity are not in fact scale-independent. Notwithstanding, the modelled point-bar lithology are broadly consistent with observations of the deposits seen along this reach (Jordan & Pryor, 1992), making the results at least applicable to river systems of Mississippi scale.

The linear relationships between meander sinuosity and facies trends used in the model are also necessary simplifications. Quantitative data and relationships describing these trends for a large number of case studies are currently lacking. Model input could be refined by incorporating more realistic relationships describing these trends from field studies across rivers at a range of scales. Furthermore, facies trends recognised in point-bar deposits and arising from variations in local flow energy around meander bends are also assumed to be linear and are implemented based on geometric rules rather than simulation of river hydrodynamics.

Even though the modelling approach allows evaluating the impact of aggradation on sand volume and distribution (*cf.* Cosma *et al.*, 2020; Yan *et al.*, 2020), channel-bed aggradation was not simulated in this study; this was done to enable isolation of the effects of planform evolution. The process of vertical aggradation would generally increase the overall thickness of point-bar deposits and overall sand volumes and fractions (Willis & Tang, 2010; Ghinassi *et al.*, 2014).

An additional limitation lies in the fact that the method used to quantify and classify the planform evolution of the modelled examples has been applied to reaches that incorporate variable numbers of meander bends, from one to four. Some of the vector (channel orientation, accretion direction, rotation) and scalar (sinuosity) quantities employed for classification are sensitive to the number of bends they are applied to; therefore, if used for scopes of comparison, it is recommended that these quantities are applied to time-lapse river planforms that include a comparable number of meander bends.

CONCLUSIONS

Based on 24 histories of river migration identified from high-resolution LiDAR images, a forward stratigraphic model, PB-SAND, has been employed to model the complex 3D sedimentary architecture and facies distributions of point-bar deposits arising from different styles of meander transformations and rotations. All point-bar cases were classified with Ward's hierarchical clustering method, applied to variables considered indicative of planform transformation mode (point-bar migration angle, apex rotation, mean sinuosity, standard deviation of channel circular variance, and preservation ratio). The three highest-

level clusters define three groups of simulations: one in which meander transformation by bend translation is dominant (group 1), and two in which bend expansion is dominant (groups 2 and 3) but which differ with respect to the average bend-apex rotation (typically higher in group 3). The modelled channel belts replicate realistic point-bar architectures and known facies trends. Modelling results incorporate bar-thickness variations caused by shifts of pool and riffle zones, fining-outward trends associated with meander expansion, and downstream-fining trends towards point-bar tails and where accretion takes place on concave benches. Three alterative trends representing different rates of facies change with sinuosity were considered in producing model outputs.

A quantitative analysis of the generated 3D models allows exploration of how bar thickness and sand thickness relate to the planform morphologies of meander-belts. These characteristics are controlled by the interplay of different facies trends and bathymetric variations. For the selected model inputs, it is observed that: (i) meander transformation styles exert a stronger impact on point-bar sand fraction than trends relating accretion-package sand proportions to sinuosity; (ii) sand vs mud fractionation between convex- and concave-bench accretion packages is the primary control on spatial variability in sand volumes; (iii) variations in sinuosity affect sand thickness primarily through bathymetric variations across pools and riffles, and secondarily through facies trends relating sand fraction to sinuosity; and (iv) changes in rotation direction of meander apices encourage abrupt changes in bar thickness and sand thickness, but the overall amount of rotation recorded in each simulation is not a strong predictor of the overall spatial variability in sand fraction.

The modelling approach taken here to draw general insight can also be used to reconstruct the likely 3D sedimentary architecture of ancient fluvial successions. It can therefore be used as a predictive tool in subsurface characterisation for cases where channel evolution can be inferred from planform morphologies of channel-belt deposits identified in seismic imagery. Although its predictive power still needs to be assessed by means of case-study applications, it is envisaged that the proposed workflow will facilitate quantitative examination of variations in facies heterogeneity and sand volumes in fluvial meander-belt successions.

ACKNOWLEDGEMENTS

The authors thank CNOOC International, Canada, for provision of financial support for development of *PB-SAND*, and FRG-ERG sponsors (AkerBP, Areva [now Orano], BHP, Cairn India [Vedanta], Chevron, ConocoPhillips, Equinor, Murphy Oil, Occidental, Saudi Aramco, Shell, Tullow Oil, Woodside, and YPF) and our partner Petrotechnical Data Systems for financial support of the research group. We thank two anonymous reviewers and Associate Editor Massimiliano Ghinassi for their constructive comments, which have improved the article.

REFERENCES

Alexander, J. (1992) Nature and origin of a laterally extensive alluvial sandstone body in the Middle Jurassic Scalby Formation. *Geol. Soc. Spec. Publ.*, **149**, 431-441.

Bhowmik, N.G. and **Demissie, M.** (1982) Bed material sorting in pools and riffles. *Journal of the Hydraulics Division, ASCE*, **108**, 1227-1231.

Bluck, B. (1971) Sedimentation in the meandering River Endrick. *Scott. J. Geol.*, **7**, 93-138.

Bridge, J.S. (2003) *Rivers and Floodplains: Forms, Processes, and Sedimentary Record.* Blackwell Publishing, Malden, 504 pp.

Bridge, J.S., Alexander, J.A.N., Collier, R.E.L., Gawthorpe, R.L. and **Jarvis, J.** (1995) Ground-penetrating radar and coring used to study the large-scale structure of point-bar deposits in three dimensions. *Sedimentology*, **42**, 839-852.

Burge, L.M. and **Smith, D.G.** (1999) Confined meandering river eddy accretions: sedimentology, channel geometry, and depositional processes. In: *Fluvial Sedimentology VI* (Eds. N.D. Smith and J. Rogers), *SEPM Spec. Publ.*, **28**, 113-130.

Clift, P.D., Olson, E.D., Lechnowskyj, A., Moran, M.G., Barbato, A. and **Lorenzo, J.M.** (2018) Grain-size variability within a mega-scale point-bar system, False River, Louisiana. *Sedimentology*, **66**. 408-434.

Colombera, L. and Mountney, N.P. (2019) The lithofacies organization of fluvial channel deposits: a meta-analysis of modern rivers. *Sediment. Geol.*, **383**, 16-40.

Colombera, L., Felletti, F., Mountney, N.P. and **McCaffrey, W.D.** (2012a) A database approach for constraining stochastic simulations of the sedimentary heterogeneity of fluvial reservoirs. *AAPG Bull.*, **96**, 2143-2166.

Colombera, L., Mountney, N.P. and McCaffrey, W.D. (2012b) A relational database for the digitization of fluvial architecture: concepts and example applications. *Pet. Geosci.*, **18**, 129-140.

Colombera, L., Mountney, N.P., Medici, G. and West, L.J. (2019) The geometry of fluvial channel bodies: empirical characterization and implications for object-based models of the subsurface. *AAPG Bull.*, **103**, 905-929.

Colombera, L., Mountney, N.P., Russell, C.E., Shiers, M.N. and McCaffrey, W.D. (2017) Geometry and compartmentalization of fluvial meander-belt reservoirs at the bar-form scale: quantitative insight from outcrop, modern and subsurface analogues. *Mar. Petrol. Geol.*, **82**, 35-55.

Colombera, L., Yan, N., McCormick-Cox, T. and **Mountney, N.P.** (2018) Seismic-driven geocellular modeling of fluvial meander-belt reservoirs using a rule-based method. *Mar. Petrol. Geol.*, **93**, 553-569.

Daniel, J.F. (1971) *Channel movement of meandering Indiana streams*. US Government Printing Office.

Deschamps, R., Guy, N., Preux, C. and **Lerat, O.** (2011) Impact of Upscaling on 3-D Modelling of SAGD in a Meander Belt, *SPE Annual Technical Conference and Exhibition.* Society of Petroleum Engineers.

Durkin, P.R. (2016) *The Evolution of Fluvial Meander Belts and Their Product in the Rock Record* [PhD. Thesis], University of Calgary, Calgary, Alberta, 245 pp.

Durkin, P.R., Hubbard, S.M., Boyd, R.L. and **Leckie, D.A.** (2015) Stratigraphic expression of intra-point-bar erosion and rotation. *J. Sediment. Res.*, **85**, 1238-1257.

Durkin, P.R., Hubbard, S.M., Smith, D.G. and **Leckie, D.A.** (2019) Predicting heterogeneity in meandering fluvial and tidal-fluvial deposits: The point bar to counter point bar transition. In: *Meandering Rivers and Their Depositional Record*. (Eds. M. Ghinassi, N. Mountney, L. Colombera and A.J. Reesink), *Spec. Publ.*, **48**, 231-250.

Finotello, A., D'Alpaos, A., Bogoni, M., Ghinassi, M. and **Lanzoni, S.** (2020) Remotely-sensed planform morphologies reveal fluvial and tidal nature of meandering channels. *Sci. Rep.*, **10**, 1-13.

Fustic, M., Hubbard, S.M., Spencer, R., Smith, D.G., Leckie, D.A., Bennett, B. and **Larter, S.** (2012) Recognition of down-valley translation in tidally influenced meandering fluvial deposits, Athabasca Oil Sands (Cretaceous), Alberta, Canada. *Mar. Petrol. Geol.*, **29**, 219-232.

Ghinassi, M. and **Ielpi, A.** (2015) Stratal Architecture and Morphodynamics of Downstream-Migrating Fluvial Point Bars (Jurassic Scalby Formation, U.K.). *J. Sediment. Res.*, **85**, 1123-1137.

Ghinassi, M., Ielpi, A., Aldinucci, M. and **Fustic, M.** (2016) Downstream-migrating fluvial point bars in the rock record. *Sediment. Geol.*, **334**, 66-96.

Ghinassi, M., Nemec, W., Aldinucci, M., Nehyba, S., Özaksoy, V. and **Fidolini, F.** (2014) Plan-form evolution of ancient meandering rivers reconstructed from longitudinal outcrop sections. *Sedimentology*, **61**, 952-977.

Hickin, E.J. (1974) The development of meanders in natural river-channels. *Am. J. Sci.*, **274**, 414-442.

Hickin, E.J. (1979) Concave-bank benches on the Squamish River, British Columbia, Canada. *Can. J. Earth Sci.*, **16**, 200-203.

Hooke, J.M. and **Yorke, L.** (2011) Channel bar dynamics on multi-decadal timescales in an active meandering river. *Earth. Surf. Proc. Land.*, **36**, 1910-1928.

Hudson, P.F. (2002) Pool-riffle morphology in an actively migrating alluvial channel: the lower Mississippi River. *Phys. Geogr.*, **23**, 154-169.

Ielpi, A. and **Ghinassi, M.** (2014) Planform architecture, stratigraphic signature and morphodynamics of an exhumed Jurassic meander plain (Scalby Formation, Yorkshire, UK). *Sedimentology*, **61**, 1923-1960.

Ielpi, A. and **Lapôtre, M.G.** (2020) A tenfold slowdown in river meander migration driven by plant life. *Nat. Geosci.*, **13**, 82-86.

Ielpi, A. and **Rainbird, R.H.** (2015) Architecture and morphodynamics of a 1·6 Ga fluvial sandstone: Ellice Formation of Elu Basin, Arctic Canada. *Sedimentology*, **62**, 1950-1977.

Jackson, R.G. (1976) Depositional model of point bars in the lower Wabash River. *J. Sediment. Res.*, **46**, 579-594.

Johnston, S. and **Holbrook, J.** (2019) Toggling between expansion and translation: The generation of a muddy-normal point bar with an earthquake imprint. In: *Meandering Rivers and Their Depositional Record*. (Eds. M. Ghinassi, N. Mountney, L. Colombera and A.J. Reesink), *Spec. Publ.*, **48**, 47-80.

Jordan, D.W. and **Pryor, W.A.** (1992). Hierarchical levels of heterogeneity in a Mississippi River meander belt and application to reservoir systems. *Am. Assoc. Petrol. Geol. Bull.*, **76**, 1601-1624.

Keller, E. and **Melhorn, W.** (1978) Rhythmic spacing and origin of pools and riffles. *Geol. Soc. Am. Bull.*, **89**, 723-730.

Konsoer, K., Zinger, J. and **Parker, G.** (2013) Bankfull hydraulic geometry of submarine channels created by turbidity currents: Relations between bankfull channel characteristics and formative flow discharge. *J. Geophys. Res. Earth Surf.*, **118**, 216-228.

Labrecque, P.A., Hubbard, S.M., Jensen, J.L. and **Nielsen, H.** (2011) Sedimentology and stratigraphic architecture of a point bar deposit, Lower Cretaceous McMurray Formation, Alberta, Canada. *Bull. Can. Pet. Geol.*, **59**, 147-171.

Lofthouse, C. and **Robert, A.** (2008) Riffle–pool sequences and meander morphology. *Geomorphology*, **99**, 214-223.

Makaske, B. and **Weerts, H.J.T.** (2005) Muddy lateral accretion and low stream power in a sub-recent confined channel belt, Rhine-Meuse delta, central Netherlands. *Sedimentology*, **52**, 651-668.

Miall, A.D. (1996) *The Geology of Fluvial Deposits*. Springer-Verlag, New York, 589 pp.

Milne, J. (1982) Bed-material size and the riffle-pool sequence. *Sedimentology*, **29**, 267-278.

Nanson, G.C. (1980) Point bar and floodplain formation of the meandering Beatton River, northeastern British Columbia, Canada. *Sedimentology*, **27**, 3-29.

Nanson, G.C. and **Page, K.** (2009) Lateral Accretion of Fine-Grained Concave Benches on Meandering Rivers, *Modern and Ancient Fluvial Systems*. Blackwell Publishing Ltd., pp. 133-143.

Nicoll, T.J. and **Hickin, E.J.** (2010) Planform geometry and channel migration of confined meandering rivers on the Canadian prairies. *Geomorphology*, **116**, 37-47.

Parquer, M., Yan, N., Colombera, L., Mountney, N.P., Collon, P. and Caumon, G. (2020) Combined inverse and forward numerical modelling for reconstruction of channel evolution and facies distributions in fluvial meander-belt deposits. *Mar. Petrol. Geol.*, **117**, 104409.

Piet, L. (1992) *Sedimentology of point bars and oxbow-fills*. University of Calgary. Alberta, Canada.

Russell, C.E., Mountney, N.P., Hodgson, D.M. and **Colombera, L.** (2019) A novel approach for prediction of lithological heterogeneity in fluvial point-bar deposits from analysis of meander morphology and scroll-bar pattern. In: *Meandering Rivers and Their Depositional Record*. (Eds. M. Ghinassi, N. Mountney, L. Colombera and A.J. Reesink), *Spec. Publ.*, **48**, 385-418.

Schwenk, J. (2016) *Meandering rivers: interpreting dynamics from planform geometry and the secret lives of migrating meanders*, University of Minnesota.

Schwenk, J., Khandelwal, A., Fratkin, M., Kumar, V. and **Foufoula-Georgiou, E.** (2017) High spatiotemporal resolution of river planform dynamics from Landsat: The RivMAP toolbox and results from the Ucayali River. *Earth Space Sci.*, **4**, 46-75.

Smith, D.G., Hubbard, S.M., Leckie, D.A. and **Fustic, M.** (2009) Counter point bar deposits: lithofacies and reservoir significance in the meandering modern Peace River and ancient McMurray Formation, Alberta, Canada. *Sedimentology*, **56**, 1655-1669.

Strick, R.J.P., Ashworth, P.J., Awcock, G. and **Lewin, J.** (2018) Morphology and spacing of river meander scrolls. *Geomorphology*, **310**, 57-68.

Taylor, G., Crook, K.A.W. and Woodyer, K.D. (1971) Upstream-dipping foreset cross-stratification; origin and implications for paleoslope analyses. *J. Sediment. Res.*, **41**, 578-581.

Thomas, R.G., Smith, D.G., Wood, J.M., Visser, J., Calverley-Range, E.A. and **Koster, E.H.** (1987) Inclined heterolithic stratification—Terminology, description, interpretation and significance. *Sediment. Geol.*, **53**, 123-179.

Thompson, A. (1986) Secondary flows and the pool-riffle unit: A case study of the processes of meander development. *Earth. Surf. Proc. Land.*, **11**, 631-641.

Tinkler, K.J. (1970) Pools, riffles, and meanders. *Geol. Soc. Am. Bull.*, **81**, 547-552.

Ward, J.J.H. (1963) Hierarchical grouping to optimize an objective function. *J. Am. Stat. Assoc.*, **58**, 236-244.

Whiting, P. J., and **Dietrich, W. E.** (1993) Experimental constraints on bar migration through bends: Implications for meander wavelength selection. *Water Resour. Res.*, **29**, 1091-1102.

Willis, B.J. and **Sech, R.P.** (2019a) Emergent facies patterns within fluvial channel belts. In: *Meandering Rivers and Their Depositional Record*. (Eds. M. Ghinassi, N. Mountney, L. Colombera and A.J. Reesink), *IAS Spec. Publ.*, **48**, 509-542.

Willis, B.J. and **Sech, R.P.** (2019b) Quantifying impacts of fluvial intra-channel-belt heterogeneity on reservoir behaviour. In: *Meandering Rivers and Their Depositional Record*. (Eds. M. Ghinassi, N. Mountney, L. Colombera and A.J. Reesink), *IAS Spec. Publ.*, **48**, 543-572.

Willis, B.J. and **Tang, H.** (2010) Three-Dimensional Connectivity of Point-Bar Deposits. *J. Sediment. Res.*, **80**, 440-454.

Wood, J.M. (1989) Alluvial architecture of the Upper Cretaceous Judith River Formation, Dinosaur Provincial Park, Alberta, Canada. *Bull. Can. Pet. Geol.*, **37**, 169-181.

Yan, N., Colombera, L., Mountney, N. and **Dorrell, R.M.** (2019) Fluvial point-bar architecture and facies heterogeneity, and their influence on intra-bar static connectivity in humid coastal-plain and dryland fan systems. In: *Meandering Rivers and Their Depositional Record*. (Eds. M. Ghinassi, N. Mountney, L. Colombera and A.J. Reesink), *Spec. Publ.*, **48**, 475–508.

Yan, N., Colombera, L. and Mountney, N.P. (2020) Three-dimensional forward stratigraphic modelling of the sedimentary architecture of meandering-river successions in evolving half-graben rift basins. *Basin Res.*, **32**, 68-90.

Yan, N., Mountney, N.P., Colombera, L. and **Dorrell, R.M.** (2017) A 3D forward stratigraphic model of fluvial meander-bend evolution for prediction of point-bar lithofacies architecture. *Comput. and Geosci.*, **105**, 65-80.

Yang, C.T. (1971) Formation of riffles and pools. *Water Resour. Res.*, **7**, 1567-1574.

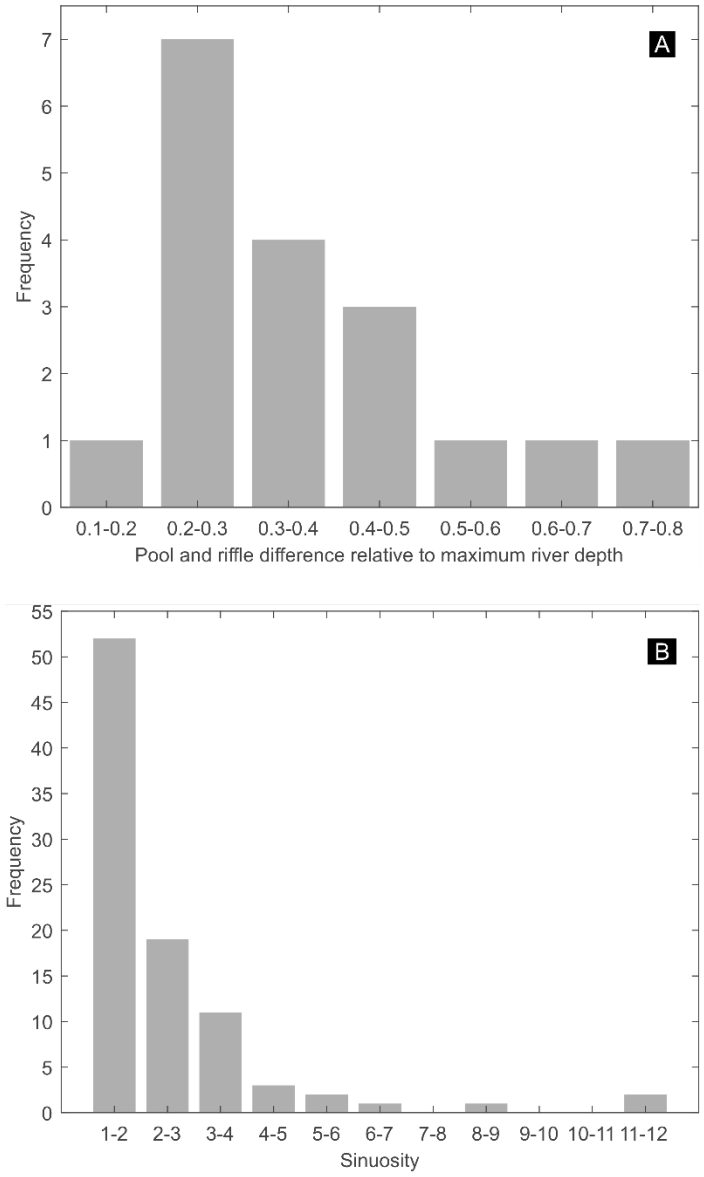

Fig. S1. (A) Histogram of pool-and-riffle depth difference, expressed relative to the maximum depth from data on the Lower Mississippi by Hudson (2002). (B) Histogram of channel sinuosity for the modelled planforms.